Appl. Phys. A (2014) 114:11–32
DOI 10.1007/s00339-013-8086-4

Applied Physics A
Materials Science & Processing

INVITED PAPER

Microscopic mechanisms of laser spallation and ablation of metal targets from large-scale molecular dynamics simulations

Chengping Wu · Leonid V. Zhigilei

Received: 4 October 2013 / Accepted: 15 October 2013 / Published online: 17 December 2013

Abstract The microscopic mechanisms of femtosecond laser ablation of an Al target are investigated in large-scale massively parallel atomistic simulations performed with a computational model combining classical molecular dynamics technique with a continuum description of the laser excitation and subsequent relaxation of conduction band electrons. The relatively large lateral size of the computational systems used in the simulations enables a detailed analysis of the evolution of multiple voids generated in a sub-surface region of the irradiated target in the spallation regime, when the material ejection is driven by the relaxation of laser-induced stresses. The nucleation, growth, and coalescence of voids take place within a broad (∼100 nm) region of the target, leading to the formation of a transient foamy structure of interconnected liquid regions and eventual separation (or spallation) of a thin liquid layer from the bulk of the target. The thickness of the spalled layer is decreasing from the maximum of ∼50 nm while the temperature and ejection velocity are increasing with increasing fluence. At a fluence of ∼2.5 times the spallation threshold, the top part of the target reaches the conditions for an explosive decomposition into vapor and small clusters/droplets, marking the transition to the phase explosion regime of laser ablation. This transition is signified by a change in the composition of the ablation plume from large liquid droplets to a mixture of vapor-phase atoms and clusters/droplets of different sizes. The clusters of different sizes are spatially segregated in the expanding ablation plume, where small/medium size clusters present in the middle of the plume are followed by slower (velocities of less than 3 km/s) large droplets consisting of more than 10,000 atoms. The similarity of some of the characteristics of laser ablation of Al targets (e.g., evolution of voids in the spallation regime and cluster size distributions in the phase explosion regime) to the ones observed in earlier simulations performed for different target materials points to the common mechanical and thermodynamic origins of the underlying processes.

C. Wu · L. V. Zhigilei (✉)
Department of Materials Science and Engineering,
University of Virginia, 395 McCormick Road, Charlottesville,
VA 22904-4745, USA
e-mail: lz2n@virginia.edu

1 Introduction

Short pulse laser ablation of metal targets is in the core of many practical applications ranging from high precision cutting and drilling [1–3], to surface nanostructuring [4–6], and to generation of nanoparticles with narrow size distribution and well-controlled composition [7–10]. The optimization of laser processing parameters in current applications and the emergence of new techniques based on laser ablation have been facilitated by computational efforts aimed at providing insights into the cascade of non-equilibrium processes triggered by the fast laser energy deposition and responsible for the material ejection [11–65]. The prominent role of computer modeling in the development of the theoretical understanding of laser-induced processes and the advancement of laser applications is defined by the complexity of the material response to the laser excitation, which includes transient modification of the material properties by strong electronic excitation, photomechanical effects driven by the relaxation of laser-induced stresses, fast non-equilibrium phase transformations occurring under conditions of rapid laser energy deposition and material expansion, ionization and plasma formation, as well as complex processes occurring in the expanding ablation plume. Computational description of this diverse range of processes is challenging and requires a combination of different computational approaches, ranging

from quantum mechanics-based (ab initio) electronic structure calculations [11–15], to classical molecular dynamics (MD) simulations [16–55], and to continuum-level kinetic and hydrodynamic modeling [56–65].

The atomistic models based on classical molecular dynamics (MD) technique, in particular, have been shown to be capable of revealing detailed information on the mechanisms of laser melting and resolidification [16–23], generation of crystal defects [24–26], photomechanical spallation [18,21,23,27–34], phase explosion and material ejection in laser ablation [17,21,23,27,32,33,35–55]. The results of MD simulations have made important contributions to the emergence of the current understanding of the interplay of the photomechanical and thermodynamic driving forces responsible for the material ejection in short pulse laser ablation, e.g., see recent reviews [66–68].

The MD simulations show that short time of the laser energy deposition can create the conditions of so-called inertial stress confinement [21,27,29], when the inability of material to expand during the time of the laser heating results in the buildup of strong compressive stresses in the surface region of the target. The relaxation of the laser-induced stresses has been shown to cause the appearance and growth of multiple sub-surface voids, leading to the eventual separation and ejection of liquid surface layer(s) or large droplets from the bulk of the target [27,29–34].

As the laser fluence increases above the spallation threshold, an abrupt change in the composition of the ejected plume, from liquid layers and large droplets to a mixture of individual atoms, atomic clusters and small droplets, has been observed in simulations and attributed to the transition from the photomechanical spallation to the phase explosion regime of material ejection [21,23,27,41]. The change in the parameters of the ejected plume upon the transition to the phase explosion regime reflects the difference in the physical mechanisms responsible for the material ejection in these two regimes: An explosive release of vapor in the liquid layer overheated above the limit of its thermodynamic stability [69–71], rather than the relaxation of photomechanical stresses, provides the main driving force for the collective ejection of the overheated layer of the target in the regime of phase explosion [21,23,47]. For longer laser pulses, when the condition for stress confinement is not satisfied and the spallation is not activated, the phase explosion has been shown to be responsible for the onset of the collective material ejection (i.e., ablation) [21,50].

While the general mechanisms of laser spallation and ablation have been well established and thoroughly investigated by now, the severe limitations on the maximum sizes of systems accessible for MD simulations limit the ability of the simulations to provide reliable quantitative data on the microscopic mechanisms of the photomechanical spallation (e.g., evolution of the void size distributions) or the dynamics of the nanoparticles formation and cluster size distributions in laser ablation. One can expect that the sizes of voids in laser spallation or nanoparticles generated in the explosive decomposition of an overheated surface layer can reach (or even exceed) the depth of the ejected material, which, in the case of metal targets, is on the order of several tens of nanometers at fluences close to the spallation/ablation thresholds. The sizes of computational cells commonly used in MD simulations of laser interactions with metal targets, however, are typically smaller than that in one [33,34,47,54,55] or both [18,21,23,29–32,35,39,43–46,51] lateral (parallel to the surface) directions. As a result, the periodic boundary conditions, typically applied in the directions parallel to the irradiated surface, do not completely eliminate the effect of the finite size of the computational cell on the simulation results, thus leaving the question on the sensitivity of the computational predictions to the size of the simulated system open.

In this paper, we report the results of large-scale massively parallel MD simulations of femtosecond laser interactions with Al target performed for large computational systems consisting of more than 10^8 atoms and having the lateral sizes comparable to the ablation depth at the highest fluence used in the simulations. The large scale of the simulations enables us to focus our analysis on two aspects of the spallation and ablation phenomena that have not been sufficiently explored so far. First, we investigate the characteristics of the evolution of sub-surface voids at laser fluences ranging from the one below the spallation threshold up to about 60 % above the spallation threshold. Second, we perform a detailed analysis of the ablation plume (including cluster size distributions, velocities and temperatures of different plume components) generated in the phase explosion irradiation regime. The results of the simulations are related to the available experimental data and computational predictions reported for different target materials.

2 Computational model

The simulations of laser spallation and ablation of a bulk Al target are performed with a combined atomistic–continuum model [18,21] that couples the classical MD method with a continuum-level description of the laser excitation and subsequent relaxation of the conduction-band electrons based on the well-known two-temperature model (TTM) [72]. In the original TTM, the time evolution of the lattice[1] and electron temperatures, T_l and T_e, is described by two coupled

[1] The use of term "lattice temperature" in this paper does not imply the preservation of the crystalline order in the system but merely follow the terminology established in the literature presenting TTM calculations, when the term lattice temperature is commonly used to refer to the temperature of the ionic subsystem that can be brought out of equilibrium

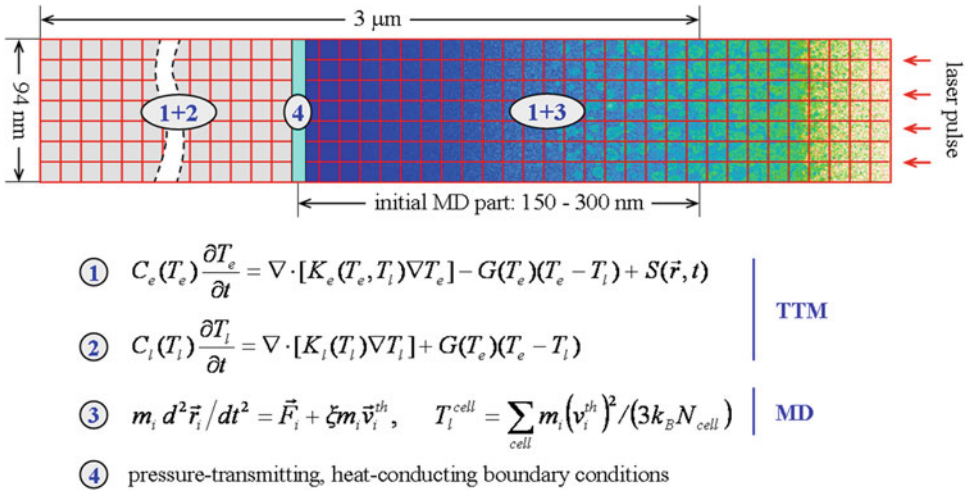

Fig. 1 Schematic of the TTM-MD model for simulation of laser interactions with metal targets. The dimensions of the computational systems used in the present simulations are shown in the figure. The laser irradiation is directed from the *right side* of the figure and periodic boundary conditions are used in the lateral (parallel to the irradiated surface) directions. Spatial discretization in the continuum part of the model and the dimensions of the atomistic and continuum regions are not drawn to scale

nonlinear differential equations that account for the electron heat conduction in the metal target and the energy exchange between the electrons and atomic vibrations. In the combined TTM-MD method, schematically illustrated in Fig. 1, MD substitutes the TTM equation for the lattice temperature in the surface region of the target, where laser-induced structural and phase transformations take place. The diffusion equation for the electron temperature, T_e, is solved on a three-dimensional (3D) grid by a finite difference method simultaneously with MD integration of the equations of motion of atoms. The cells in the 3D finite difference discretization are related to the corresponding volumes of the MD system, and the local lattice temperature, T_l^{cell}, is defined for each cell from the average kinetic energy of thermal motion of atoms. The electron temperature enters a coupling term, $\xi m_i \vec{v}_i^{\,\text{th}}$, that is added to the MD equations of motion (see Fig. 1) to account for the energy exchange between the electrons and the lattice. In this coupling term, ξ is a coefficient that depends on the instantaneous difference between the local lattice and electron temperatures [18], m_i is the mass of an atom i, $\vec{v}_i^{\,\text{th}}$ is the thermal velocity of the atom defined as $\vec{v}_i^{\,\text{th}} = \vec{v}_i - \vec{v}^{\,\text{c}}$, where $\vec{v}_i$ is the actual velocity of atom i and $\vec{v}^{\,\text{c}}$ is the velocity of the center of mass of a cell to which the atom i belongs. The expansion, density variation and, at higher fluences, disintegration of the irradiated target predicted in the MD part of the model are accounted for through the corresponding changes of the parameters of the TTM equation for electron temperature. In the continuum part of the model, beyond the surface region represented by the MD method, the electronic heat conduction and the energy exchange between the electrons and the lattice are described by the conventional TTM equations for the electron and lattice temperatures. A more detailed description of the TTM-MD model is provided in Refs. [18,21].

In the simulations reported in this paper, the MD part of the TTM-MD model represents the top 150 nm surface region of a single crystal Al target irradiated at an absorbed laser fluence of 650 J/m^2 (below the spallation threshold), the top 200 nm region at fluences from 750 to 1,100 J/m^2 (in the spallation regime), and the top 300 nm region at a higher fluence of 2000 J/m^2 (in the phase explosion regime). These values of depth of the MD region are chosen so that the processes of melting, spallation and ablation are confined within the MD part of the model. The lateral dimensions of the MD computational systems are 94 nm × 94 nm, with the 150, 200 and 300 nm systems composed of about 77, 107 and 159 million atoms, respectively. Periodic boundary conditions are applied in the lateral directions, parallel to the top (001) free surfaces of the initial fcc crystals. A dynamic pressure-transmitting boundary condition is applied at the bottom of MD system [73,74] to ensure non-reflecting propagation of the laser-induced stress wave from the MD part of the model into the bulk of the target. Before applying laser irradiation, the MD systems are equilibrated at 300 K and the dimensions of the MD computational cells are chosen so that the initial targets are free of internal stresses.

While one-dimensional (1D) solutions of the diffusion equation for T_e were used in some of the earlier TTM-MD simulations performed for systems with smaller lateral sizes of the computational systems [21,23,29], a 3D solution is necessary to adequately represent the electronic heat transfer in the larger-scale simulations, where large density variations at the initial stage of the spallation or ablation process may create conditions for complex 3D heat flow in the surface regions of the irradiated targets. Thus, in this work, the TTM equation for the electron temperature in the TTM-MD part of the system is solved on a 3D grid with the cell size of 3 nm × 3 nm × 1 nm. The smaller dimension of 1 nm is used in the direction normal to the surface to provide an ade-

Footnote 1 continued
with the conduction-band electrons by short pulse laser irradiation. At high laser fluences the melting process may take place before the complete electron-phonon equilibration.

quate treatment of the strong electron temperature gradient generated by the laser excitation. In the continuum part of the model, beyond the surface region represented by the MD method, the conventional TTM equations for the electron and lattice temperatures are solved on a 3D computational grid with twice larger spacing in the direction normal to the surface. The continuum region is extended down to the depth of 3 μm, so that no significant changes in the electron and lattice temperatures are observed at the bottom of the computational domain during the time of the simulations.

The interatomic interaction in the MD part of the model is described by the embedded atom method (EAM) potential with the functional form and parameterization developed for Al in Ref. [75]. Although this potential is fitted to low-temperature properties of Al (cohesive energy, elastic constants, phonon dispersion relations, energies of point and planar crystal defects), it also provides a good description of high-temperature thermodynamic properties of the material relevant to the conditions of the simulations reported in this work. In particular, the melting temperature determined in liquid–crystal coexistence simulations is reported to be 1,042 K [76], about 12 % above the experimental value. The temperature and pressure conditions for the onset of the explosive phase separation into liquid and vapor (or cavitation at large negative pressure), T^* and P^*, are determined for the EAM Al in a series of constant-pressure MD simulations of a slow (0.2 K/ps) heating of a metastable liquid, following an approach applied earlier to other material systems [21,23,48,71]. The onset of the phase explosion is identified from a sharp increase in volume of the system and the threshold temperature for the phase explosion is found to be about 5,600 K at zero pressure and about 6,400 K at 0.2 GPa. The onset of the phase explosion can be expected at ∼10 % below the critical temperature [69–71] and the calculated values are consistent with experimental value of the critical temperature of Al ranging from 4,700 to 9,500 K [77,78], with an average value of 6,700 K "recommended" in a recent review [78]. Comparable values have also been predicted in recent thermodynamic calculations performed for other EAM potentials for Al [79]. In the calculations performed for negative values of pressure, the limit of stability of the metastable liquid against the onset of the cavitation (sharp increase in volume of the computational system) is found to be 4,120 K at −0.5 GPa, 3,250 K at −1.0 GPa, and 2,600 K at −1.5 GPa.

The electron temperature dependences of the thermophysical material properties included in the TTM equation for the electron temperature (electron-phonon coupling factor and electron heat capacity) are taken in the forms that account for the thermal excitation from the electron states below the Fermi level [13,80]. The electron thermal conductivity is described by the Drude model relationship, $K_e(T_e, T_l) = v^2 C_e(T_e)\tau_e(T_e, T_l)/3$, where $C_e(T_e)$ is the electron heat capacity, v^2 is the mean square velocity of the electrons contributing to the electron heat conductivity, approximated in this work as the Fermi velocity squared, v_F^2, and $\tau_e(T_e, T_l)$ is the total electron scattering time defined by the electron–electron and electron–phonon scattering rates, $1/\tau_e = 1/\tau_{e-e} + 1/\tau_{e-ph} = AT_e^2 + BT_l$. The value of the coefficient A, 1.39×10^6 s^{-1} K^{-2}, is estimated within the free electron model, following the approach suggested in [81]. The value of the coefficient B, 5.924×10^{11} s^{-1} K^{-1} is obtained from the experimental value of the thermal conductivity of solid Al at the melting temperature, 211 Wm^{-1} K^{-1} [82].

The irradiation of the target with a 100 fs laser pulse is represented through a source term added to the equation for the electron temperature [18]. The source term simulates excitation of the conduction band electrons by a laser pulse with a Gaussian temporal profile and reproduces the exponential attenuation of laser intensity with depth under the surface (Beer–Lambert law). To account for the energy transport occurring before the thermalization of the excited electrons [83,84], the optical absorption depth, $L_p = 8$ nm at laser wavelength of 800 nm [85,86], is combined with the effective depth of the "ballistic" energy transport, $L_b = 16$ nm, roughly estimated here as a product of the Fermi velocity and the Drude relaxation time [87]. The effective range of the laser energy deposition is then defined as $L_p + L_b = 24$ nm and is used in the source term instead of L_p alone [18,26,84]. The reflectivity of the surface is not defined in the model since the absorbed laser fluence rather than the incident fluence is used in the discussion of the simulation results.

3 Mechanisms of photomechanical spallation

A detailed analysis of the microscopic mechanisms of photomechanical spallation is performed in this work based on the results of four large-scale TTM-MD simulations. The visual picture of the dynamic response of the surface region of the irradiated target to the fast laser energy deposition is provided in series of snapshots from the simulations shown in Fig. 2. The appearance and growth of sub-surface voids are observed in all simulations illustrated in Fig. 2. At the lowest fluence of 650 J/m^2, the generation of voids does not lead to the material ejection from the target. A single void is formed in this simulation at a depth of ∼60 nm by coalescence of two adjacent voids at about 90 ps. The void increases in size up to the time of about 350 ps and starts to shrink after that time (see inset in Fig. 2a). In three other simulations performed at laser fluences of 750 J/m^2 and above, the growth, coalescence and percolation of multiple voids result in the formation of complex structures of interconnected liquid regions and eventual separation (or spallation) of thin liquid layers from the tar-

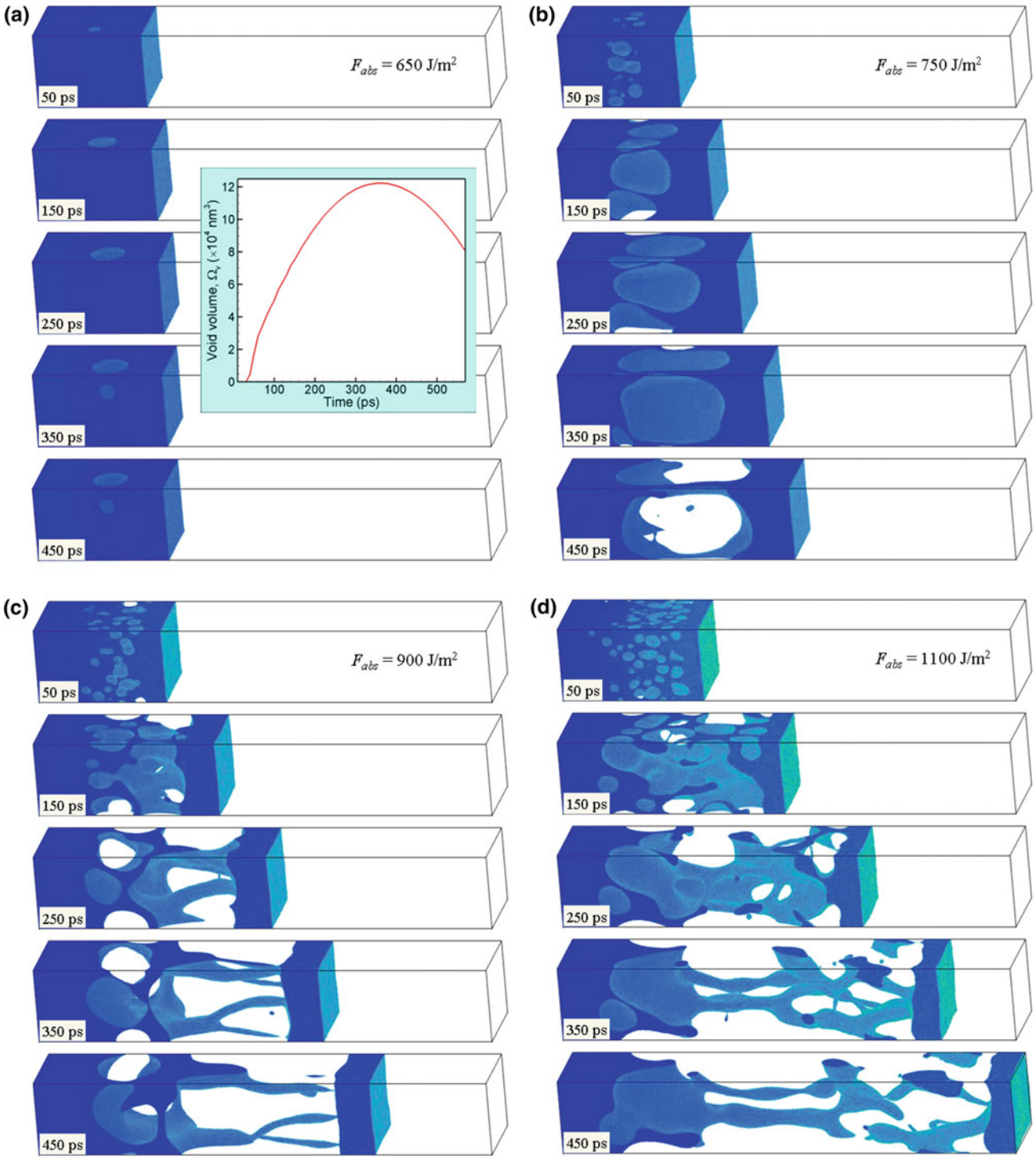

Fig. 2 Snapshots of atomic configurations predicted in TTM-MD simulations of laser spallation of bulk Al targets irradiated by 100 fs laser pulses at absorbed fluences of 650 J/m^2 (**a**), 750 J/m^2 (**b**), 900 J/m^2 (**c**), and 1,100 J/m^2 (**d**). The laser irradiation is directed from the *right* side of the figure. The *inset* in **a** shows the evolution of the total volume of voids in a simulation performed at a fluence of 650 J/m^2. Only *top* parts of the computational systems, from −115 to 450 nm with respect to the initial surface of the target, are shown in the snapshots. The atoms are *colored* according to their potential energies

gets. Note that in the initial test simulations performed with systems of smaller lateral dimensions (4 nm × 4 nm), the spallation threshold was somewhat higher, with spallation occurring at 750 J/m^2, but no void nucleation observed at 650 or 700 J/m^2. This observation can be explained by the lower probability of nucleation of a void of a critical size

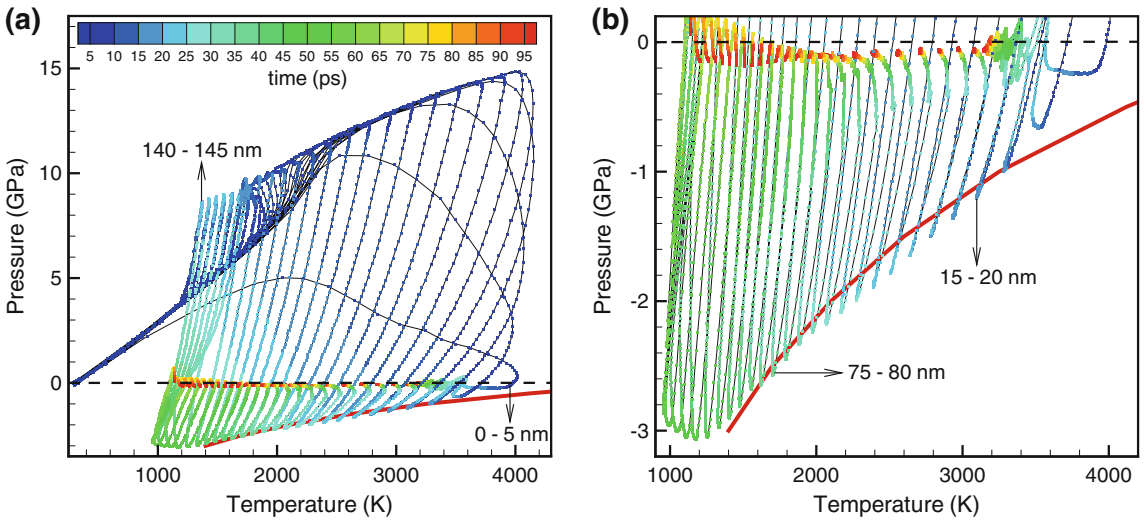

Fig. 3 The evolution of temperature and pressure averaged over 5 nm thick consecutive layers located at different depths in the initial target in a simulation illustrated in Fig. 2d. The *red curve* shows the temperature–pressure conditions (T^*, P^*) for the onset of the cavitation or phase explosion in the metastable liquid, calculated for the EAM Al material as explained in Sect. 2

in a smaller computational cell during the fast evolution of the laser-induced stresses, as well as the increased nucleation stress due to the elastic interaction of a nucleating void with itself across the periodic boundaries (this process corresponds to a simultaneous nucleation of an array of voids). Similar lateral size dependence has been observed for nucleation of voids in an Al crystal under conditions of high strain rate tensile loading [88].

The photomechanical nature of the spallation process is evident from Fig. 3, where the evolution of pressure and temperature is shown for 5 nm thick layers located at different depths in the initial target in a consecutive order. The initial increase in temperature and pressure in different layers, Fig. 3a, follows similar path that is defined by the rapid heating due to the laser excitation and electron–phonon energy transfer taking place under conditions of constant volume (stress confinement). The degree of the stress confinement is different in different layers, with the top layers starting to expand before the electron–phonon equilibration is completed, thus reducing the maximum pressure reached in these layers. As a result, the maximum compressive pressure of 15 GPa is reached in the fifth layer located between 20 and 25 nm in the initial target. The buildup of compressive pressure is followed by a rapid drop in pressure which, for layers below 20 nm, coincides with the passage of the unloading component of the stress wave generated due to the relaxation of the laser-induced compressive stresses in the presence of the free surface of the target [29]. In all layers, the unloading wave turns the compressive stresses into tensile ones, with the maximum tensile stresses increasing with depth down to the layer located between 110 and 115 nm. Importantly, the temperature–pressure trajectories for layers located between 15 and 80 nm cross the red line showing the limit of the stability of the metastable liquid against the onset of the cavitation, Fig. 3b. These are also the layers where the void formation is observed in the simulation, thus pointing to the photomechanical driving forces responsible for the ejection of liquid layers in the spallation regime. Note that the temperature-pressure trajectories of the top two layers do not cross the "red line" and these two layers are not affected by the void nucleation, see Fig. 2d.

Following the spallation, a relatively slow collapse/flattening of the foamy liquid structures generated between the spalled layers and the remaining targets (Fig. 2b-d) proceeds simultaneously with cooling and resolidification of the surface regions of the targets. Although the simulations were not continued until the complete solidification of the surface, we can speculate that the solidification process may result in freezing of some of the surface structures and lead to the formation of complex nanoscale surface morphology commonly observed in femtosecond laser processing experiments [4–6]. In the case of the transient appearance of voids below the spallation threshold, observed at 650 J/m^2 (Fig. 2a), the voids can be captured by the solidification front [68], leading to an effective "swelling" of the surface region of the irradiated target. This effect of "swelling" or "frustrated ablation" [89], as well as direct observation of the formation of sub-surface nano-voids [34], has recently been reported for Al targets irradiated by 100 fs laser pulses.

A more detailed picture of the initial stage of the void evolution is provided in the snapshots shown in Fig. 4, where each void is represented by a spherical particle with the same volume as the actual void. The voids are identified by superimposing atomic configurations with a 3D grid of cubic cells with a size of 0.39 nm, finding the cells that do not contain any atoms, and defining the voids as clusters of adja-

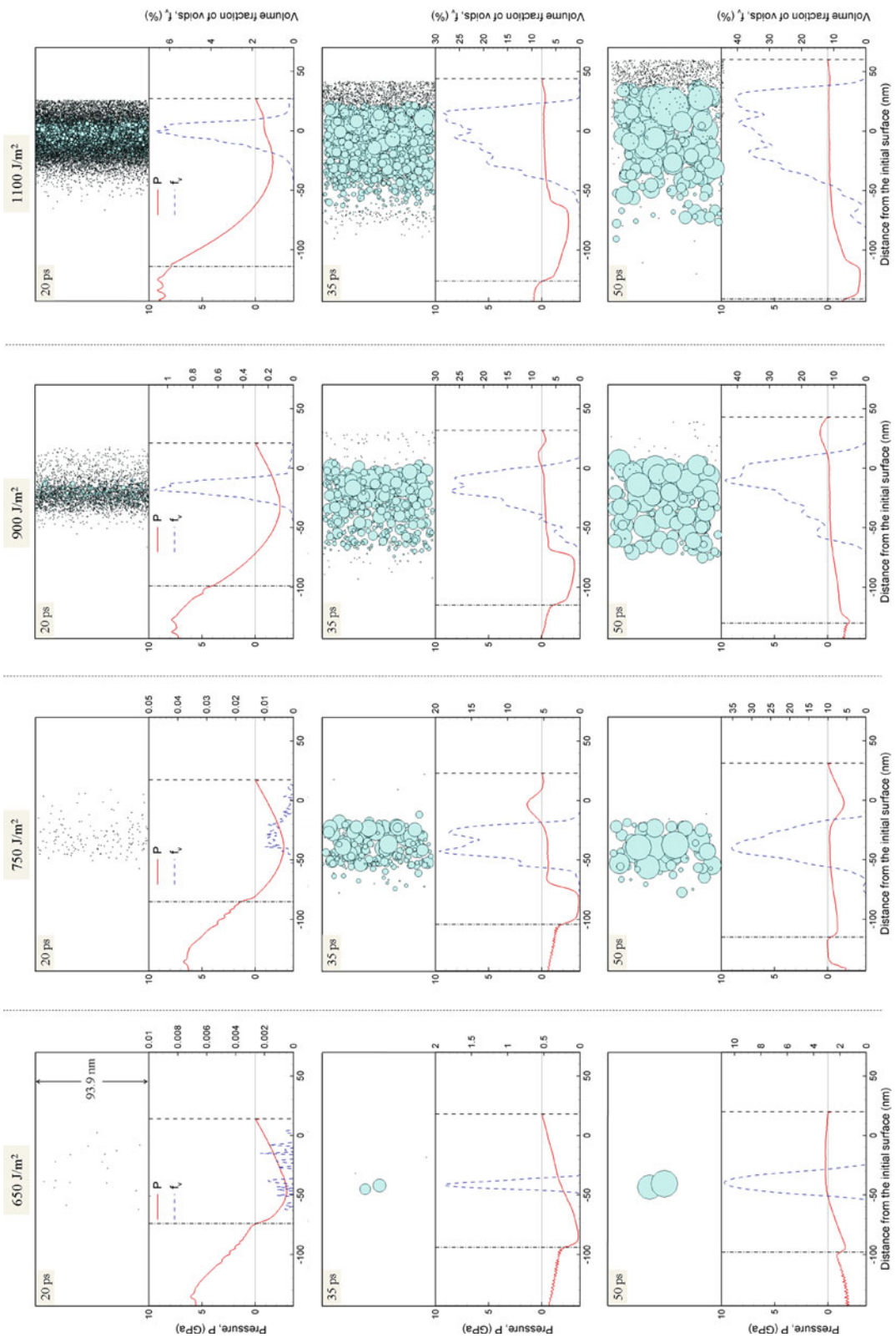

Fig. 4 The distributions of voids, pressure and volume fraction of voids predicted in simulations illustrated by snapshots in Fig. 2 for times of 20, 35, and 50 ps after the laser pulse. In the *upper* parts of the frames, the voids are represented by *spheres* of the same volume as the actual voids. The *dashed lines* show current positions of the surface, and the *dash-dotted lines* show current positions of the melting front. Similarly to Figs. 1 and 2, the laser irradiation is directed from the *right* side of the frames. Note the differences in the scales of the volume fractions of voids used in different frames

cent empty cells. The smallest voids, therefore, correspond to clusters of two neighboring empty cells. The appearance and growth of the voids are correlated in Fig. 4 with the generation and propagation of laser-induced stress wave. As discussed in a number of earlier publications, e.g. [21,27,29], it is the relaxation of the laser-induced stresses that provides the driving force for the nucleation and growth of the subsurface voids leading to the spallation. The energy transfer from the excited electrons to the atomic vibrations results in a rapid heating and a buildup of high compressive stresses in the surface region of the target. The relaxation of the compressive stresses in the presence of free surface induces the collective motion of the top surface region away from the bulk of the target and leads to the formation of an unloading tensile component of the stress wave that follows the compressive one in its propagation from the surface to the bulk of the target.

In the simulations illustrated in Fig. 2, the tensile stresses are sufficiently strong to induce nucleation and growth of multiple voids in the surface region of the irradiated targets. The appearance of voids coincides with the time of the raise of the tensile stresses in the melted part of the target, as can be seen from the pressure plots and snapshots shown in Fig. 4 for 20 ps. The number of small voids and the width of the region of void nucleation are increasing with increasing laser fluence, even though the maximum tensile stresses observed at higher fluences are smaller. This observation can be explained by the temperature dependence of the ability of the melted material to withstand the transient tensile stresses. The temperature of the melted surface region increases with increasing fluence and the dissipation of the tensile component of the stress wave results in the generation of more numerous voids over a wider part of the melted region.

Two peculiarities of the pressure profiles can be noted in Fig. 4. First, there is a pronounced stepwise increase in pressure across the liquid–solid interface. This increase is related to the inability of the thermoelastic compressive stresses generated in the crystalline part of the target to completely relax by the uniaxial expansion in the direction normal to the surface [21,30]. In the melted part of the target, the stresses remain isotropic during the expansion of the surface region and the pressure variations are defined by the dynamics of the pressure wave. The uniaxial expansion of the crystalline part of the target, however, results in anisotropic lattice deformations and corresponding anisotropic compressive stresses. As a result, the pressure profiles in the solid parts of the targets are defined by superposition of the pressure waves with the background of the quasi-static compressive stresses. Second, a partial reflection of a tail of the tensile component of the pressure wave from the quickly emerging low-density region of the void evolution results in periodic oscillations of pressure in the topmost layer of the target, as can be seen in the profiles shown for 35 and 50 ps for simulations performed at laser fluences of 750 and 900 J/m^2. At 1,100 J/m^2, the liquid layer between the voids and the free surface of the target is too shallow and has too high temperature to support any noticeable elastic oscillations.

After the peak of the tensile stresses associated with the unloading wave moves away from the region of the void nucleation, the number of small voids starts to drop, whereas larger voids appear, grow and coalesce, as shown in the snapshots for 35 and 50 ps in Fig. 4. While in the case of 650 J/m^2 only two voids are observed at 50 ps, at higher fluences the voids form a continuous region of reduced density that expands with time as the top liquid layer accelerated by the relaxation of the laser-induced stresses moves away from the target. By the time of 50 ps, the maximum volume fraction of voids reaches 35 % in the simulation performed at 750 J/m^2 and 40 % at 900 and 1,100 J/m^2. The maximum fraction of voids continues to increase in these simulations and reaches 100 % at the time when the last liquid bridge connecting the layer to the bulk of the target breaks (Fig. 2).

The visual analysis of the void nucleation and growth provided above can be complemented by quantitative evaluation of the void size distributions. The distributions are calculated for different times during the simulations and are found to be relatively well described by a power law dependence, $N_v(V) \sim V^{-\tau}$, where V is the void volume and -τ is power law exponent that is increasing with time. Despite the differences in the dynamics of the spallation process, the time evolutions of the void size distributions calculated for fluences of 750, 900, and 1,100 J/m^2 are similar to each other. A representative set of distributions is shown in Fig. 5a for 1,100 J/m^2. The plots of the time dependences of the power law exponents shown for these three simulations in Fig. 5b highlight the lack of sensitivity of the evolution of the void size distributions to the laser fluence. The sharp increase of the power law exponents during the first 40 ps is reflecting the active process of void coarsening and coalescence, when the size and the number of large voids are growing at the expense of quickly decreasing population of small voids. The power law void size distributions shown in Fig. 5a are similar to the ones observed in earlier simulations of laser spallation of a Ni film [30] and bulk molecular targets [29], as well as in a simulation of back-surface spallation of Ta [90]. This similarity is indicative of the common physical origin of the processes of void nucleation, growth and coalescence responsible for the spallation of different materials.

The distinct stages of the void evolution can also be identified from the plots of the total number of voids and total volume of voids shown in Fig. 6. The sharp spikes of the total number of voids during the first ~25 ps after the laser pulse reflect the expansion of the surface regions, generation of tensile stresses, and appearance of a large number of small empty regions which, with the definition of "voids" described above, are counted as individual voids but make

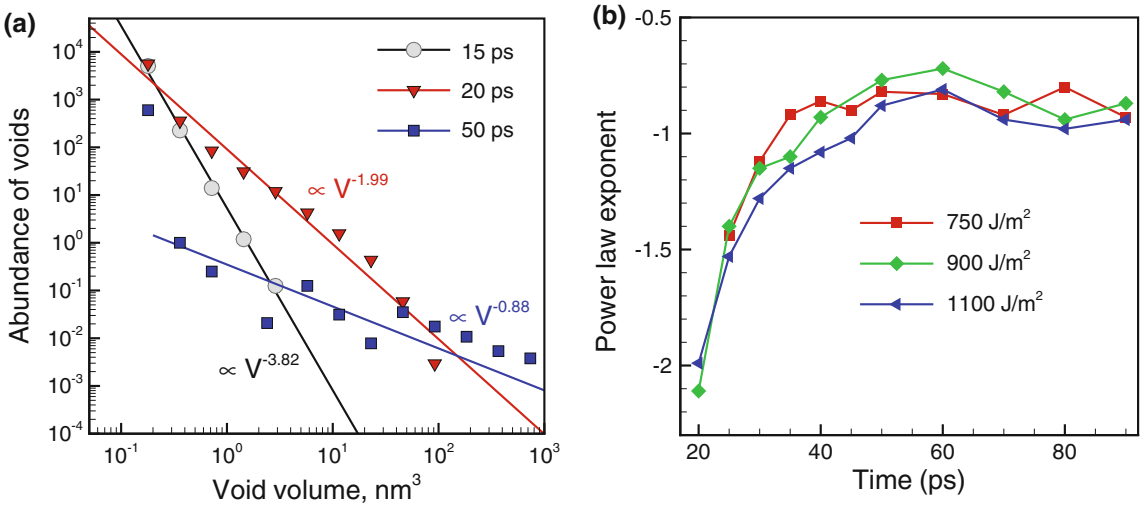

Fig. 5 Void abundance distributions as functions of void volume predicted for different times in a simulation of 100 fs laser irradiation of an Al target at an absorbed laser fluence of 1,100 J/m^2 (**a**) and the time evolution of power-law exponents calculated by fitting the data obtained in simulations performed at absorbed fluences of 750, 900, and 1,100 J/m^2 to power law dependences (**b**). The *lines* in **a** are power law fits of the data points with the exponents indicated in the figure

up a very small total volume of voids (e.g., at 20 ps, when the total number of voids is at its maximum). The growth of some of the empty regions leads to the emergence of larger voids, which relax the tensile stresses in the surrounding liquid (Fig. 4), resulting in the sharp decrease in the population of the small voids. After 40 ps, the growth and coalescence of the large voids are reflected in the steady increase in the total volume of voids and slow decrease in the number of voids.

The practically important outcome of the generation and growth of the sub-surface voids discussed in details above is the separation and ejection of a liquid layer from the irradiated target. The parameters of the spalled layers are shown in Fig. 7, where the ejection velocity, thickness, and temperature of the spalled layers are shown. As discussed above, the initial acceleration of the surface layer in the direction away from the target (positive velocity in Fig. 7a) is the result of the relaxation of the laser-induced compressive stresses. It is followed by the deceleration associated with the generation of the tensile stresses in the surface region of the target. In contrast to thermo-elastic material response to the laser heating [91,92], however, the fast deceleration is interrupted by the generation of voids that reflects the inability of the melted layer to support the quickly evolving tensile stresses. The porous regions with large volume fractions of voids generated by the time of ~30–40 ps, Fig. 4, have weak resistance to the uniaxial extension and cannot significantly reduce the outward velocity of the top liquid layers in the simulations performed at fluences of 750 J/m^2 and higher. The porous liquid regions in these simulations evolve into extended foamy structures of interconnected liquid regions that eventually break and disconnect from the spalled layers, releasing the layers to free flights away from the targets (the times of the complete separation of the spalled layers from the targets are marked by cross symbols in Fig. 7a for two of the simulations). At 650 J/m^2, however, the region with only two voids generated during the initial relaxation of the laser-induced stresses provides enough resistance to the uniaxial extension to slow down the outward motion of the top surface layer and to reverse the direction of its motion, thus preventing spallation of the layer. The range of velocities of the spalled layers predicted in the simulations, from ~300 m/s close to the spallation threshold to ~1,000 m/s at a laser fluence about 60 % above the spallation thresholds, is consistent with the values estimated from the changes of interference patterns (Newton rings) with time following femtosecond laser irradiation of different target materials [93–95].

For the three simulations where the spallation occurs, the dependences of the thickness and temperature of the spalled layers on laser fluence are shown in Fig. 7b. The thickness of the spalled layer decreases by about a factor of two, from 50 to 24 nm, and the temperature increases from about 1,700 K to more than 3,000 K as the fluence increases from 750 to 1,100 J/m^2. While in MD simulations the spalled layers are stabilized by the periodic boundary conditions and cannot be expected to lose their integrity if the simulations are continued for longer time, in experiments the spalled layers will eventually decompose into individual droplets. The size of the droplets can be roughly estimated from the conclusions of a theoretical analysis of the stability of thin free liquid films [96] that predicts the following expression for the dominant perturbation wavelength that leads to spontaneous rupture of the film: $\Lambda(h) = [(8\pi^3\gamma)/A_H]^{1/2}h^2$, where h is the film thickness, γ is the surface energy of liquid Al, and A_H is the Hamaker constant. Assuming that a circular section of the film with a volume of a cylinder with diameter Λ and

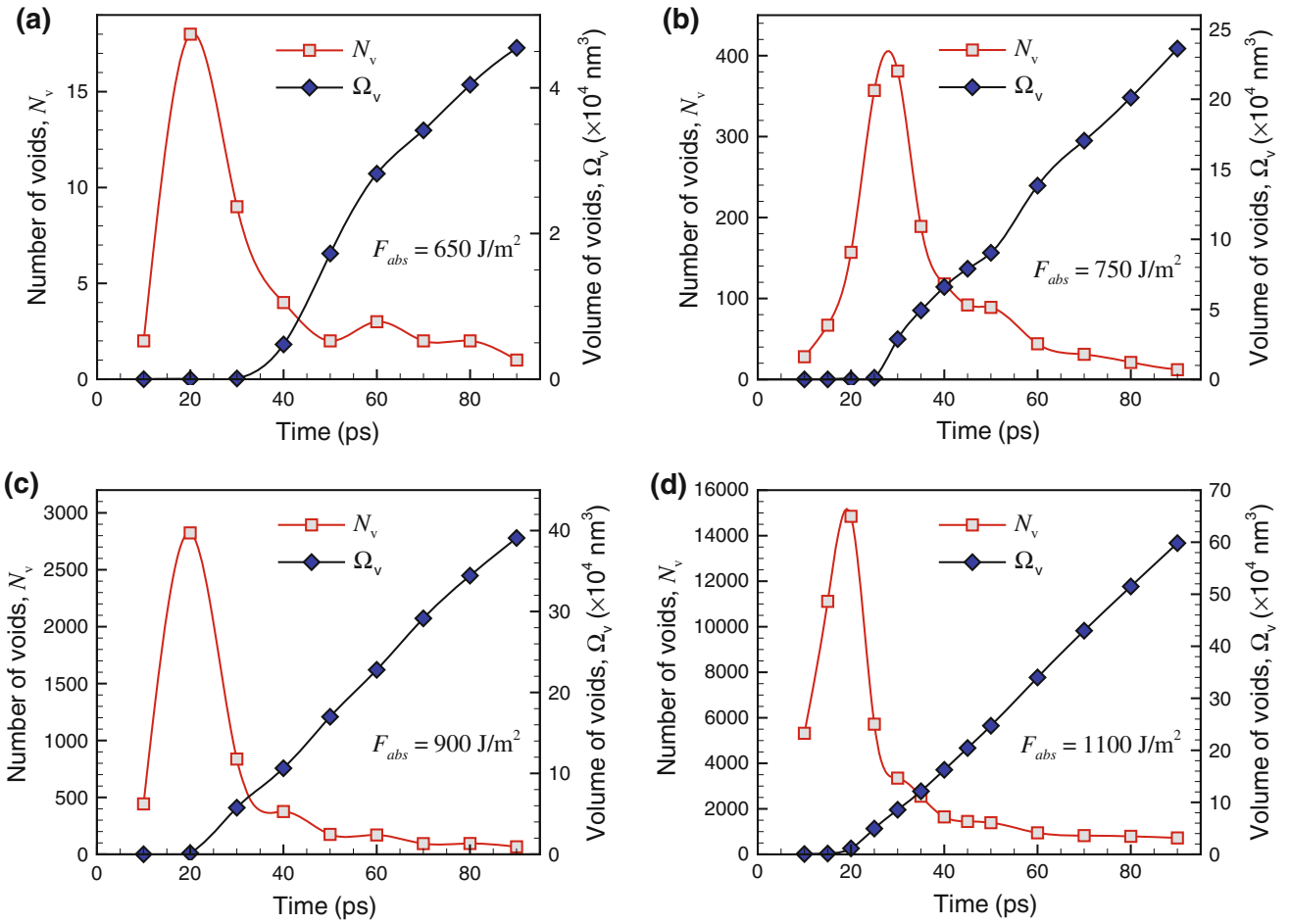

Fig. 6 The evolution of the total number of voids N_v (with voids defined as explained in the text) and the total volume of voids Ω_v at the initial stage of the spallation process in simulations of 100 fs laser irradiation of Al targets at absorbed fluences of 650 J/m^2 (**a**), 750 J/m^2 (**b**), 900 J/m^2 (**c**), and 1,100 J/m^2 (**d**)

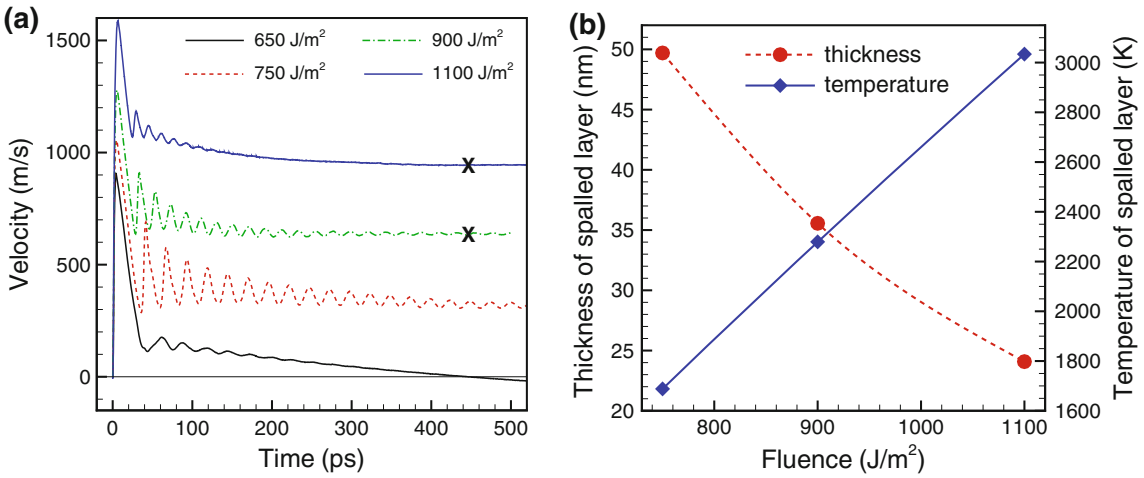

Fig. 7 The time dependence of the collective velocity of the top surface regions of Al targets irradiated with 100 fs laser pulses at fluences of 650, 750, 900, and 1,100 J/m^2 (**a**) and the thickness and temperature of the spalled layers ejected in three of these simulations (**b**). In **a**, the collective velocities are calculated for atoms that belong to the top 4 nm layers of the initial targets, the *thin horizontal line* marks zero velocity, and the cross signs indicate the time of complete spallation of the top surface layer. In **b**, the thickness of the spalled layer is expressed in units of the corresponding thickness of the initial solid Al target at 300 K (a layer of this thickness in the initial target has the number of atoms equal to those in the spalled layer)

thickness h contributes to one spherical droplet, the droplet diameter can be estimated as $d = [(12\pi^3\gamma)/A_H]^{1/3}h^{5/3}$.

For a liquid Al film, Λ and d can be evaluated using the Hamaker constant, $A_H = 3.6 \times 10^{-19}$ J [97], and a semi-empirical equation for the temperature dependence of the surface energy of liquid metals [98], $\gamma = \gamma_0(1 - T/T_c)^{1.2}$, that ensures that the energy of the liquid-vapor interface vanishes at the critical temperature T_c. The parameter $\gamma_0 = 1,036\,\mathrm{mJ/m^2}$ is determined using the values of the surface energy of liquid Al at the melting temperature T_m = 933 K, $\gamma(T_m) = 865\,\mathrm{mJ/m^2}$ [98], and the critical temperature $T_c = 6,700$ K [78]. With all the parameters defined above and the temperature and thickness of the spalled layers provided in Fig. 7b, the values of Λ and d can now be evaluated as $\Lambda = 55.4\,\mu\mathrm{m}$ and $d = 6.1\,\mu\mathrm{m}$ for 750 J/m^2, $\Lambda = 26.3\,\mu\mathrm{m}$ and $d = 3.3\,\mu\mathrm{m}$ for 900 J/m^2, and $\Lambda = 10.8\,\mu\mathrm{m}$ and $d = 1.6\,\mu\mathrm{m}$ for 1,100 J/m^2.

With the estimates of Λ being on the order of a typical laser spot size used in laser material processing experiments, it is clear that the above-mentioned stability analysis can only provide a significantly overestimated upper bound value of the maximum size of droplets emerging from the decomposition of the liquid layers separated from the target in the spallation regime. The instabilities related to the process of separation of the layer from the extended foamy liquid structures bridging the spalled layer with the bulk of the target, as well as the spatial variation of the thickness of the layer within the laser spot, is likely to induce decomposition of the layer at a scale smaller than Λ. Thus, the characteristic size of the droplets ejected in laser spallation is likely to be on the scale of 100s of nanometers to micrometers.

4 Mechanisms of laser ablation in the phase explosion regime

The almost linear increase of temperature of the spalled layer with increasing fluence observed in Fig. 7b allows us to roughly estimate the fluence at which the maximum temperature of the surface region of the target would reach the range of temperatures $T^* = 5,600$–$6,400$ K identified in Sect. 2 as the threshold temperatures for the onset of the explosive phase separation into liquid and vapor at positive values of pressure. The linear extrapolation of the temperature of the spalled layer to T^* yields an estimate of about 1,800 J/m^2 for the absorbed fluence required for the onset of the phase explosion. The dependence of the thickness of the spalled layer shown in Fig. 7b also suggests that the layer will vanish by this fluence. Therefore, the large-scale simulation of laser ablation in the phase explosion regime is performed in this work at an absorbed fluence of 2,000 J/m^2, $\geq$10 % above the threshold for the transition from the spallation to phase explosion regimes of laser ablation.

The visual picture of the material ejection at $F_{abs} = 2,000$ J/m^2, in the phase explosion regime, is shown in Fig. 8. In the first snapshot, shown for 50 ps after the laser pulse, one can see a fine "Swiss cheese"-like cellular structure generated in ~100 nm wide surface region of the target. In the top part of this region, the cellular structure is generated by a rapid (explosive) release of vapor in the melted metal overheated up to the threshold temperature for phase explosion. The conditions leading to the explosive phase separation are illustrated in Fig. 9, where temperature–pressure trajectories of the material initially located in different layers below the surface are shown. The trajectories are similar to the ones discussed in Sect. 3 for the simulation performed in the spallation regime, at 1,100 J/m^2, Fig. 3. The difference, however, is in the higher temperature of the top region of the target which approaches (and even exceeds) the critical temperature of the material. The relaxation of the laser-induced pressure in this case makes the trajectories for the top layers cross the "red line" at high temperatures and low magnitudes of negative pressure (or even at positive pressure, as shown for the three top 1 nm thick layers in Fig. 9c). The material ejection in this case proceeds through the rapid decomposition into liquid and vapor and leads to the fast cooling of the mixture. Note that the conditions in each layer do not correspond to the thermodynamic equilibrium, particularly during the rapid expansion of the layers and the explosive phase separation. Therefore, we do not call the curves shown in Fig. 9 "thermodynamic trajectories" to avoid misinterpretation. After the onset of the phase explosion, the pressure–temperature trajectories show the average temperature and pressure of the vapor and liquid components of the mixtures which, in general, are not in thermal equilibrium with each other.

Deeper into the target, the propagation of the tensile component of the stress wave leads to the additional cavitation in the superheated liquid, with the density of vapor in the pores decreasing with depth. The trajectories for the material initially located at the depth up to 100 nm (Fig. 9b) cross the red line that defines the limit of the stability of the metastable liquid against the onset of the cavitation at large negative stresses, suggesting that the relaxation of the tensile stresses rather than the release of vapor-phase atoms provides the main driving force for the formation and growth of voids in this region.

The expansion of the cellular structure leads to the coarsening of the liquid and vapor regions and results in the formation of a foamy structure of interconnected liquid regions extending in the direction of the plume expansion (see snapshots for 150–450 ps in Fig. 8). The liquid regions are surrounded by vapor in the top part of the expanding foamy structure, whereas the large voids generated in the deeper regions of the target are virtually free of vapor. This observation corroborates the above discussion of the dominant driving forces responsible for the material decomposition in

different parts of the irradiated targets. The eventual decomposition of the complex hierarchical foamy structure into individual liquid droplets, atomic clusters and vapor-phase atoms leads to the formation of a multi-component ablation plume moving away from the target.

5 Phase explosion regime of laser ablation: parameters of the plume

The snapshots shown in Fig. 8 illustrate the laser-induced processes occurring in the close vicinity of the initial surface of the irradiated target. To provide a broader view of the ablation plume, a snapshot for 630 ps after the laser pulse is shown in Fig. 10 as a sequence of three consecutive fragments covering a range from −300 nm below the level of the initial surface of the target up to 2.7 μm above the initial surface. A prominent characteristic of the ablation plume apparent from Fig. 10 is the spatial segregation of clusters/droplets of different sizes. The vapor-phase atoms and small clusters are predominantly present in the front part of the expanding plume (Fig. 10c), the medium size clusters are localized in the middle of the expanding plume (Fig. 10b), and the large liquid droplets can be expected to emerge as final products of the slow process of decomposition of the extended liquid structures that is still ongoing at the time of 630 ps (Fig. 10a).

This visual analysis can be supported by quantitative data on the spatial distributions of different plume components shown for the same time of 630 ps in Fig. 11. The plot of the flow velocities in the direction away from the target, shown in Fig. 12, can be used to determine the local flow velocities of different parts of the spatial distributions shown in Fig. 11. The individual atoms and small 2–10 atom clusters have distributions that peak at ∼1.4 μm and have shapes defined by the free expansion of the vapor generated in the phase explosion. The expansion proceeds both in the direction away from the target and toward the target, by percolation through the foamy structure of liquid regions, Fig. 11a, b. The resistance of the transient foamy structure to the expansion of the vapor is manifested in a clear break in the dependence of the flow velocity of vapor-phase atoms on the distance from the initial surface at ∼1.6 μm from the surface, Fig. 12. The maximum velocity of the vapor-phase atoms exceeds 9,500 m/s, whereas maximum velocity of small (≤10 atoms) clusters is ∼8,000 m/s.

Most of the clusters with sizes of 11–100 atoms are also formed in the phase explosion of the top region of the target and are moving with velocities of ∼2,000–6,000 m/s in the front part of the plume. The spatial distributions for larger clusters/droplets shift closer to the target with increasing size and the droplets consisting of more than 10,000 atoms (droplets with diameters larger than 7 nm) are found only in the region below 1.6 μm, see Figs. 10b and 11e. From Fig. 12 we see that the flow velocity of these droplets is ranging from 1,000 to 3,000 m/s. Finally, the large extended liquid regions present in the tail of the expanding plume (Fig. 10a) can be expected to separate from the target and form large droplets with sizes comparable to the lateral dimensions of the com-

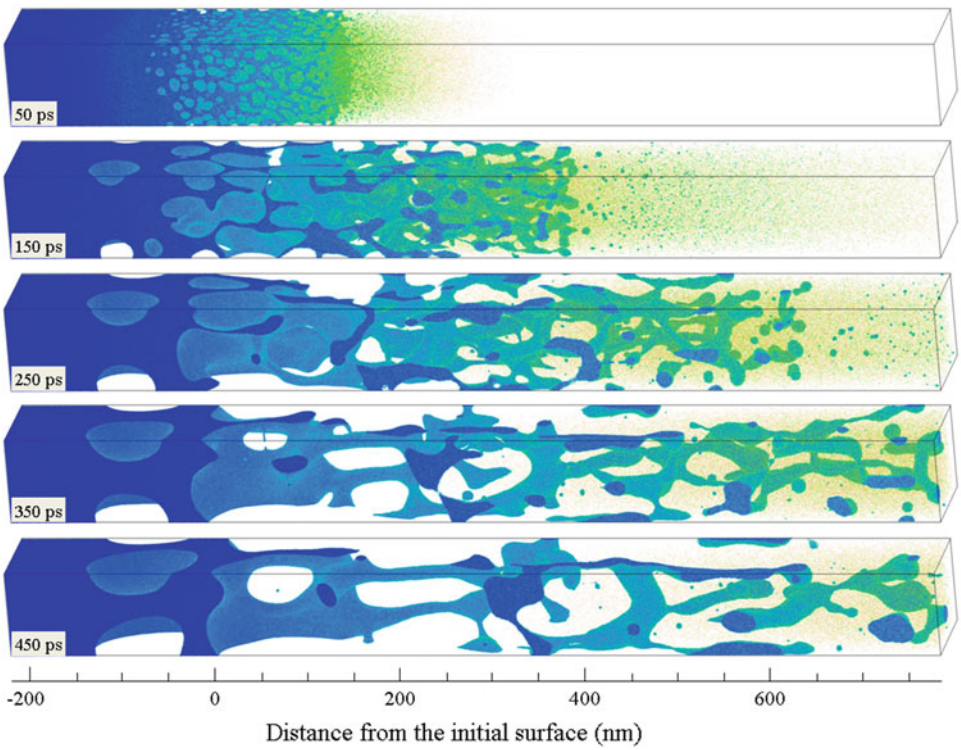

Fig. 8 Snapshots of atomic configurations predicted in TTM-MD simulation of laser ablation of a bulk Al target irradiated by a 100 fs laser pulse at an absorbed fluence of 2,000 J/m^2. The irradiation regime in this simulation corresponds to the phase explosion and ablation of a surface region of the target. Only parts of the computational system are shown in the snapshots. The atoms are *colored* according to their potential energies

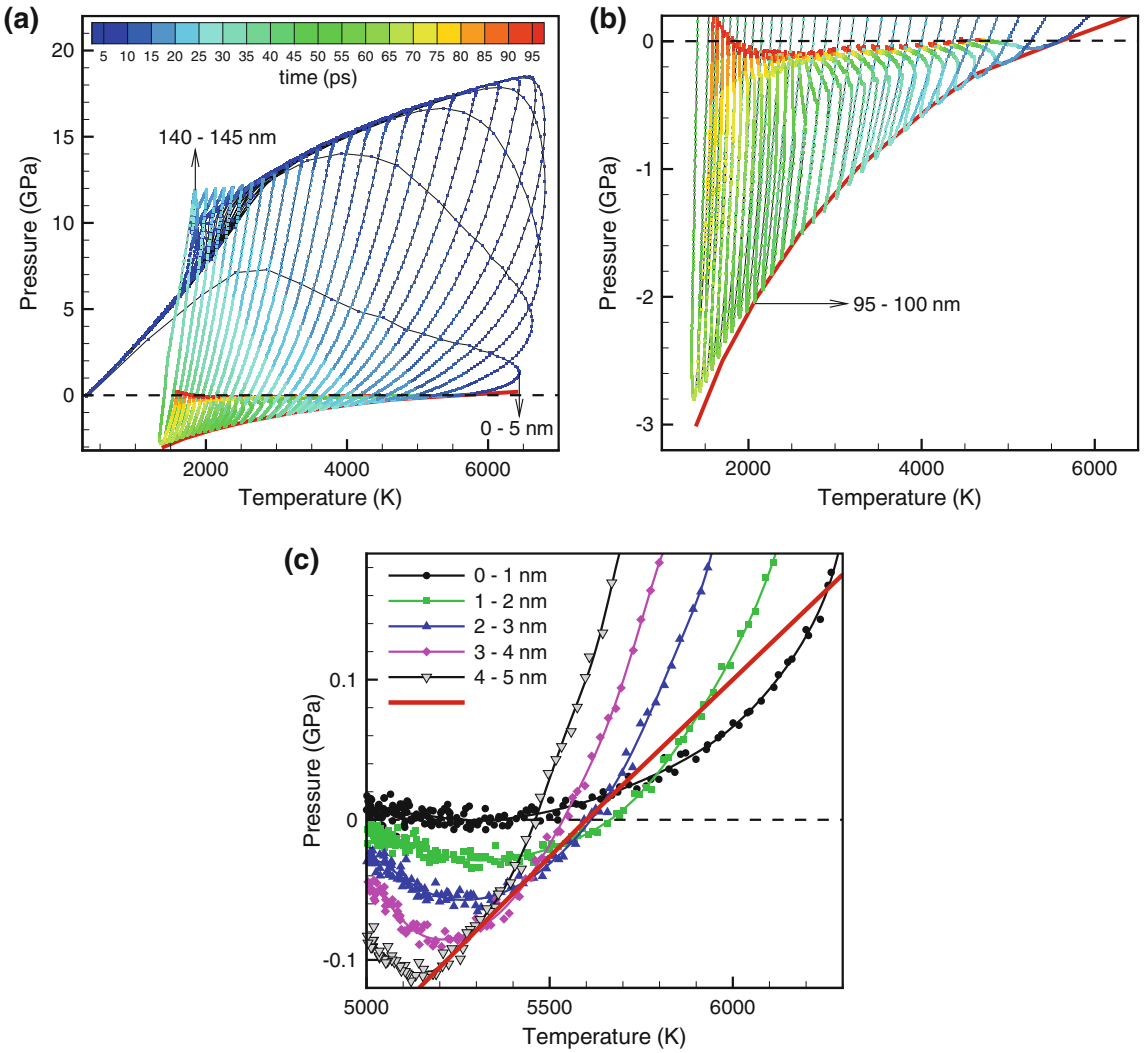

Fig. 9 The evolution of temperature and pressure averaged over 5 nm thick (**a**, **b**) or 1 nm thick (**c**) consecutive layers located at different depths in the initial target in a simulation illustrated in Fig. 8. The *red curve* shows the temperature–pressure conditions (T^*, P^*) for the onset of the cavitation or phase explosion in the metastable liquid, calculated for the EAM Al material as explained in Sect. 2

putational cell, 100 nm. The velocities of these droplets are likely to be on the order of 100s of m/s.

The effect of the spatial segregation of clusters and droplets of different sizes in the ablation plume has been observed in earlier MD [27,40,41,46,48,99] and combined MD—Direct Simulation Monte Carlo (DSMC) [100–103] simulations of laser ablation of molecular systems and metals. Detailed analysis of the physical origin of this effect, performed for irradiation conditions that correspond to the absence [40] and presence [99] of stress confinement, has revealed variation of the mechanisms of the cluster formation with the depth of origin (and the energy density deposited by the laser pulse) of the material contributing to different parts of the ablation plume. The plots of temperature–pressure trajectories in Fig. 9 confirm this assessment and suggest that, under conditions of stress confinement realized in femtosecond laser ablation of metals, the clusters and droplets generated in the phase explosion of the top part of the target and the ones emerging from photomechanical cavitation and disintegration of the deeper melted material have different characteristics and contribute to different parts of the ablation plume.

The spatial segregation of different plume components predicted in the simulations can be related to the results of plume imaging experiments [46,100,104–108], where splitting of the plume into a fast component with optical emission characteristic for neutral atoms and a slow component with blackbody-like emission associated with presence of hot clusters is observed. The plume separation into the fast ($\sim 10^4$ m/s) vapor-phase component followed by slower ($\sim 10^3$ m/s) nanoparticles is also inferred from the results of spatial- and time-resolved soft X-ray absorption

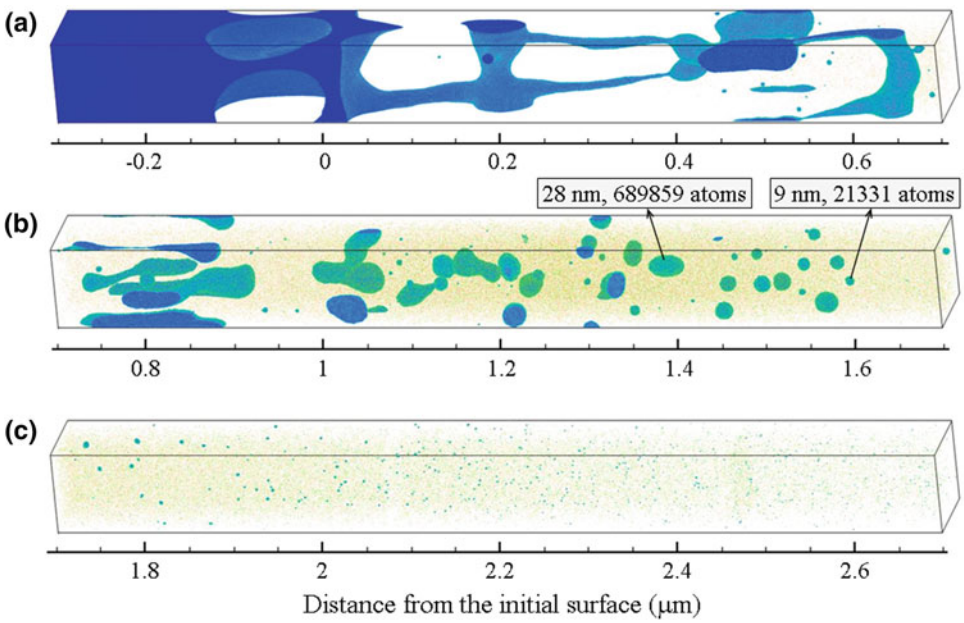

Fig. 10 Snapshot of the atomic configuration predicted in the simulation illustrated by Fig. 8 for a time of 630 ps after the laser pulse. To provide a broader view of the ablation plume, the snapshot is shown as a sequence of three consecutive fragments covering a range from −300 nm below the level of the initial surface of the target up to 2.7 μm above the surface. The atoms are *colored* according to their potential energies. The effective diameter and number of atoms are indicated in **b** for two representative droplets

spectroscopy probing of plumes generated in 100 fs laser ablation of Al targets [109,110]. The characteristic velocities of the vapor and nanoparticle components of the ablation plumes deduced from the plume imaging experiments are in a good quantitative agreement with the computational predictions. An observation of a similar layered structure of the plume (vaporized layer followed by small particles and larger droplets) in nanosecond laser ablation of water and soft tissue [111] highlights the general character of the plume segregation effect in short pulse laser ablation of different target materials.

The mass fractions of different plume components, defined as the number of atoms constituting the clusters within the corresponding size ranges divided by the total number of atoms in the ablation plume, are indicated in Fig. 11. The liquid regions that are still connected to the bulk of the target (Fig. 10a) are not included in the calculation of the mass fractions. The striking result of this analysis is the very small fractions of the vapor-phase atoms (2.3 wt.%) and small atomic clusters (3.8 wt.% for the range from dimers to 10,000 atom clusters). The dominant contribution to the mass of the ablation plume is made by liquid droplets consisting of more than 10,000 atoms (diameters larger than 7 nm). This observation is consistent with experimental data suggesting that the nanoparticles constitute a major fraction of the total mass of ejected material in femtosecond laser ablation of metals [106,112], as well as with the results of earlier smaller-scale MD simulations, where the mass fraction of the vapor-phase atoms in the total yield is observed to be ∼4 wt.% for Cr [23] and ∼10 wt.% for Ni [21] just above the threshold for transition from the spallation to the phase explosion regime of laser ablation.

To characterize the overall cluster composition of the ablation plume, the cluster size distribution is shown in Fig. 13. In the distribution plotted in double-logarithmic scale one can distinguish three distinct regions that correspond to the vapor-phase atoms and 2–4 atom clusters, small clusters consisting of 5–20 atoms, and larger clusters. The cluster size distributions in each of these regions can be described by a power law $Y(N) \sim N^{-\tau}$ with different exponents. The decay of the probability to find clusters of increasingly larger size is substantially slower in the high-mass part of the distribution and the absolute value of the exponent is more than twice smaller compared to the one for small clusters.

The distributions similar to the one shown in Fig. 13 have been observed in earlier simulations performed for one-component molecular targets [40] and polymer solutions [48,52]. The bi-modal size distributions for molecular systems are characterized by power-law exponents ranging from −1.6 to −1.1 for large clusters and −4.1 to −3.5 for small clusters consisting of less than 20 molecules. In experiments, power law mass distributions of surface features have been observed in polymer films deposited by matrix-assisted pulsed laser evaporation (MAPLE) technique [113,114], where the power law exponents of −1.65 [113] and −2 [114] have been evaluated from SEM analysis of surface morphology of the deposited films. These values are close to the ones predicted for the high-mass clusters in the simulations. In recent mass spectrometry measurements of clusters ejected in laser ablation of sinapinic acid targets [115], bimodal power law distributions with exponents of −2 for clusters consisting of more than ten molecules and −2.8 for smaller clusters and monomers are reported. The semi-quantitative consistency of the cluster size distributions

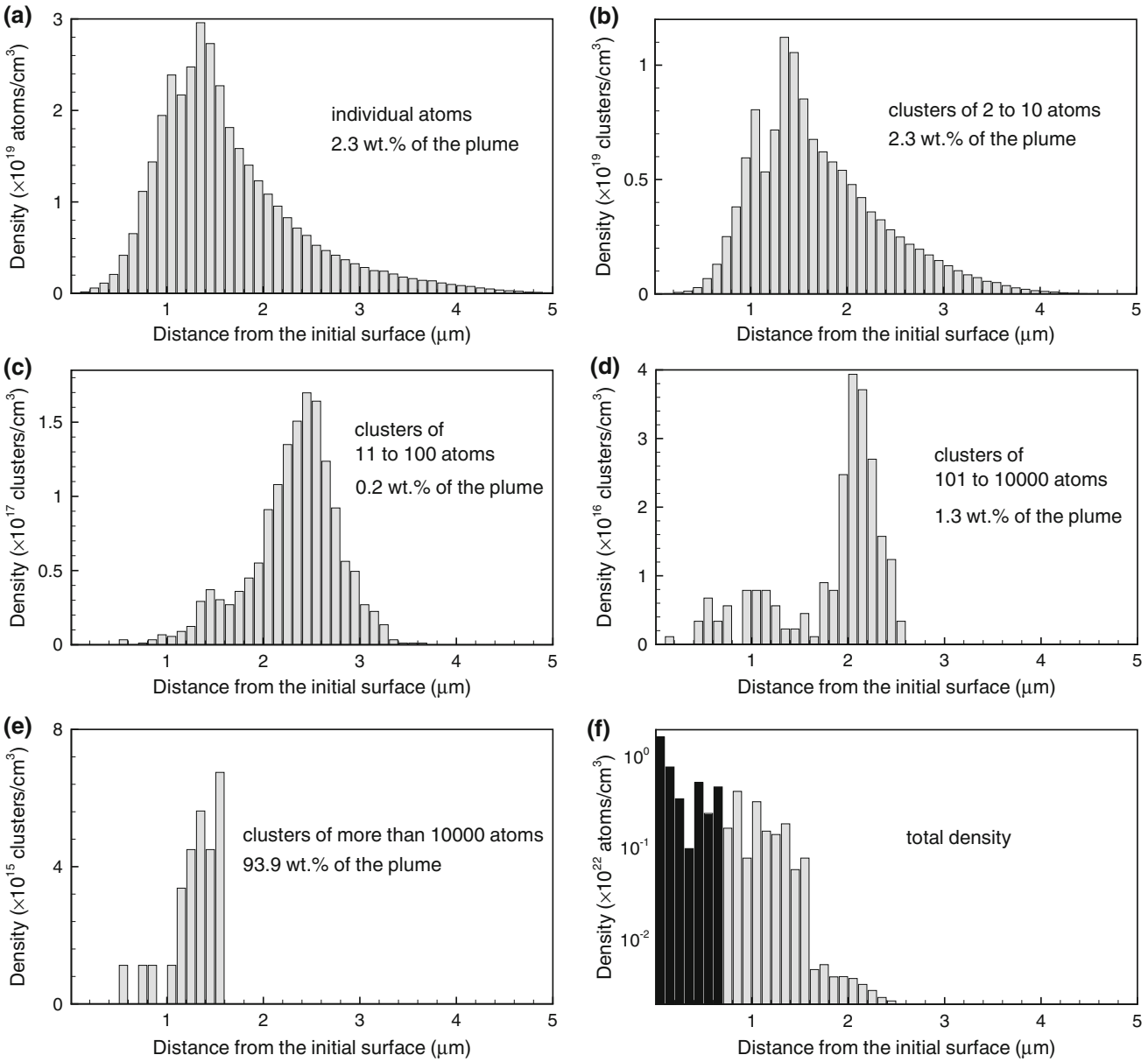

Fig. 11 Number density of individual atoms (**a**), clusters of different sizes (**b**–**e**) and the total density above the location of the initial surface (**f**) as a function of the distance from the initial surface in a simulation of laser ablation of a bulk Al target irradiated by a 100 fs laser pulse at an absorbed fluence of 2,000 J/m^2. The data are for 630 ps after the laser pulse, with a corresponding snapshot of the plume shown in Fig. 10. The distributions are plotted for groups of clusters to obtain statistically adequate representations of the spatial distribution of clusters of different sizes in the ablation plume. The mass fractions of the different plume components in the ejected plume are indicated in the corresponding plots. The contribution of the liquid regions still connected to the bulk of the target at 630 ps (but likely to separate at a later time) to the density distribution is shown by *black bars* in **e** and is not included in the calculation of the mass of the ejected plume

reported for different target materials and a broad range of irradiation conditions suggests that the bi-modal power law cluster size distribution may be a general characteristic of ablation plumes ejected in the regime of phase explosion.

The complexity and highly non-equilibrium character of the ablation process make it difficult to establish direct links to the existing theoretical models that predict power-law cluster size distributions, such as the gas–liquid phase transition occurring at the critical point [116], various mechanical fragmentation processes [117–119], and particle emission due to the shock wave interaction with a surface [120–122]. The existence of the two, low- and high-mass, regions in the cluster size distributions, however, suggests that the small and large clusters in laser ablation have different origins. The majority of individual atoms and small clusters are released in the explosive decomposition of the strongly superheated

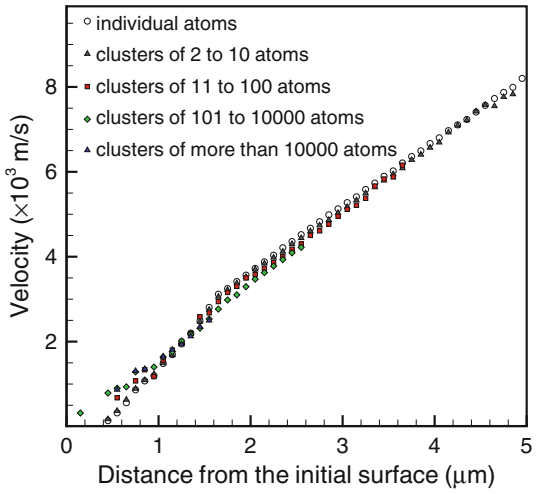

Fig. 12 Flow velocity of different plume components in the direction normal to the irradiated surface as a function of the distance from the initial surface. The data is shown for 630 ps after irradiation with a 100 fs laser pulse at an absorbed fluence of 2,000 J/m^2

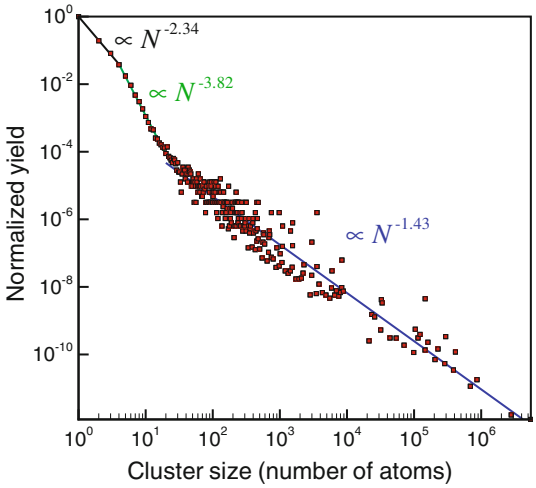

Fig. 13 Cluster size distributions in the ablation plume generated by the time of 630 ps in a simulation of 100 fs laser pulse irradiation of a bulk Al target at an absorbed fluence of 2,000 J/m^2. The lines are power law fits of the data points in three regions that correspond to the individual atoms and 2–4 atom clusters, clusters consisting of 5–20 atoms, and larger clusters. The corresponding power-law dependences are indicated in the plot

top part of the target, whereas the larger clusters appear as a result of disintegration and coarsening of the transient liquid structure of interconnected liquid regions, as illustrated in Fig. 8.

To describe the temperature of different plume components, two characteristics, the translational and internal temperatures, are calculated from the instantaneous atomic velocities at 630 ps after the laser pulse. The translational temperature is calculated for vapor-phase atoms and clusters of different sizes from the radial (parallel to the surface of the irradiated target) components of the velocities of atoms or center of mass velocities of clusters. The values of local translational temperature, shown in Fig. 14a, are obtained by averaging over atoms or clusters located at different distances from the irradiated surface. The radial velocity components do not contain a contribution from the flow of the plume away from the irradiated target and can be associated with the thermal motion of atoms and clusters in the plume [27,40]. The results of the calculation, however, show that the local equilibration is achieved only for small clusters that consist of up to ten atoms, as shown in Fig. 14a. The values of local translational temperature for larger clusters (not shown in the figure) exhibit considerable scatter due to the limited statistics and tend to be significantly higher than the temperature of the surrounding vapor. The higher translational temperatures of the large clusters suggest that the clusters acquire relatively high radial velocities in the process of the explosive formation of the ablation plume and have not experienced a number of collisions with vapor-phase atoms and smaller clusters that would be sufficient for local thermal equilibration.

In addition to the local translational temperature, the internal temperatures of clusters of different sizes are calculated from the kinetic energies of atomic motion in the cluster center of mass frame of reference. Since the translational degrees of freedom of clusters are excluded from the calculation of the kinetic energies, the internal temperature of a cluster of n atoms, $T_{\rm int}^{(n)}$, is obtained by equating the kinetic energy to $\frac{3}{2}(n-1)k_{\rm B}T_{\rm int}^{(n)}$. The dependence of the local internal temperature on the distance from the irradiated surface is shown in Fig. 14b and the cluster size dependence is shown in Fig. 15.

A significant variation of the translational and internal temperatures with distance from the irradiated surface, Fig. 14a, b, as well as a strong correlation of the internal temperature with the size of a cluster (larger clusters have, on average, higher internal temperature), Fig. 15, reflects the dependence of the plume cooling efficiency on the local energy density deposited by the laser pulse. The stronger overheating of the upper part of the ablation plume leads to a more vigorous phase explosion with a larger fraction of the released vapor-phase atoms, a faster expansion, and a more efficient cooling, as compared to a slower evaporative cooling of the large droplets ejected in the tail of the plume. Similar cooling behavior and the corresponding distributions of the translational and internal temperatures have been observed in earlier simulations performed for molecular systems [27,40,41].

The value of the internal temperature of ~4,000 K observed in the simulation for large clusters/droplets, Fig. 15, and the decrease of translational (Fig. 14a) and internal (Fig. 14b) temperatures of the clusters with increasing distance from the target are consistent with experimental data reported for the same system, Al target irradiated by 100 fs

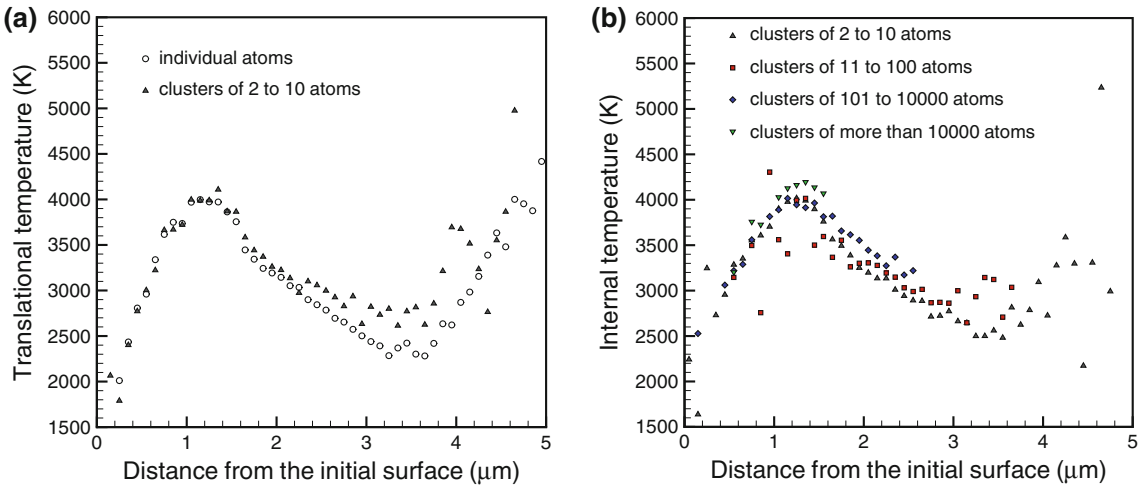

Fig. 14 Translational (**a**) and internal (**b**) temperatures of different plume components as functions of the distance from the surface. The translational temperature is calculated from the velocity components of the ejected atoms or clusters in the direction parallel to the irradiated surface. The internal temperature is calculated from the kinetic energies of atomic motion in the clusters' center of mass frame of reference. The data are shown for 630 ps after irradiation with a 100 fs laser pulse at an absorbed fluence of 2,000 J/m^2

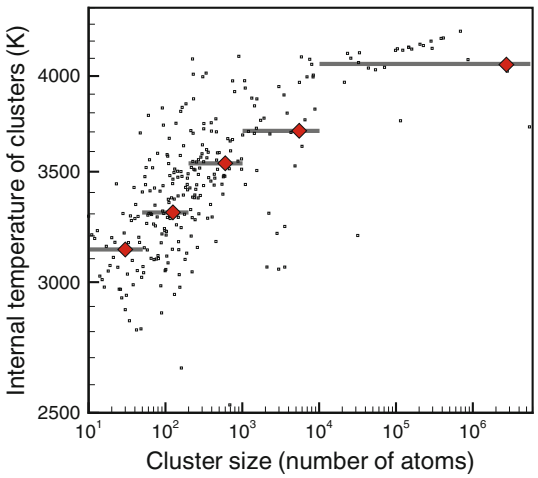

Fig. 15 Internal temperature of clusters of different sizes. *Small dots* show the average temperature of clusters with specific number of atoms and five *large diamonds* show the average temperatures of clusters that belong to the following ranges of sizes (marked by *dark bars*): from 10 to 50, from 50 to 200, from 200 to 1,000, from 1,000 to 10,000, and larger than 10,000. The data are shown for 630 ps after irradiation with a 100 fs laser pulse at an absorbed fluence of 2,000 J/m^2

laser pulse [110]. The temperatures measured in the experiments for a time delay of 30 ns after the laser pulse range from ∼3,800–4,500 K at ∼5 μm from the surface and decrease with increasing distance from the irradiated target.

6 A "big picture" of laser ablation for a Gaussian laser beam

The severe limitations on the length scales accessible with MD method make it impossible to directly simulate processes occurring at the scale of the whole laser spot. As discussed in Sect. 1, the MD computational cell is assumed to represent a local volume within the laser spot, i.e., any effects related to the lateral variations of the laser energy deposition are neglected and the periodic boundary conditions are used to reproduce the interaction of atoms in the MD computational cell with the surrounding material. The information on the material ejection from the whole laser spot, however, can still be obtained by combining the results of a series of MD simulations performed for a range of local fluences. This "mosaic approach" to representation of the laser-induced processes at the scale of the whole laser spot is illustrated in Fig. 16 for a Gaussian shape of the laser beam profile with the standard deviation σ and a peak absorbed laser fluence of 2,050 J/m^2. The peak fluence is slightly above the threshold for the transition from the spallation to phase explosion ablation regime.

The snapshots used in Fig. 16 are from the simulations discussed above, in Sects. 3–5, as well as two additional simulations performed at 1,450 and 1,750 J/m^2. All snapshots are taken at the same time of 150 ps after the 100 fs laser pulse irradiation. The conditions in these simulations correspond to local laser fluences realized at different distances from the center of the Gaussian laser beam profile. The snapshots are aligned with locations that correspond to the values of local fluence used in the simulations, as shown by the vertical and horizontal dashed lines, respectively. The locations of the melting front at 150 ps are shown by red dots and the thicknesses and locations of the top void-free layers are shown by black bars. Note that the lengths of the black bars show the estimates of the final thickness of the spalled layers after their separation (spallation) from the target for the simulations where the spallation takes place. For the sim-

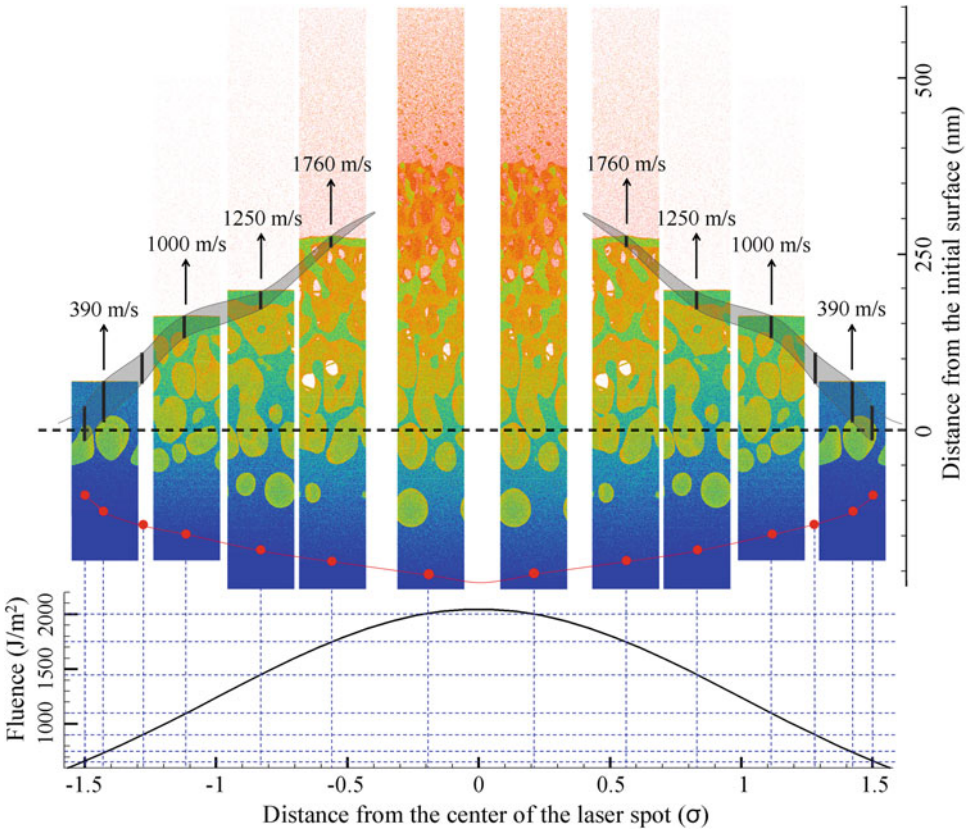

Fig. 16 The integral visual picture of melting, generation of subsurface voids and material ejection from an Al target irradiated by a 100 fs laser pulse. The laser beam has a Gaussian spatial profile with a peak absorbed laser fluence of 2,050 J/m^2, as shown in the *bottom* part of the figure. The representation of the laser-induced processes at the scale of the whole laser spot is based on a "mosaic approach", where snapshots from individual TTM-MD simulations taken at the same time of 150 ps after the laser pulse are aligned with locations within the laser spot that correspond to the values of local fluence used in the simulations, as shown by the thin *vertical* and *horizontal dashed lines*. The atoms in the snapshots are *colored* by their potential energy, from *blue* for low energy atoms in the bulk of the target to *red* for the vapor-phase atoms. The *red dots* connected by the *red line* mark the location of the melting front. The thicknesses and locations of the top void-free layers are shown by *black bars* for simulations performed in the spallation regime and, in the case of the lowest fluence of 650 J/m^2, just below the spallation threshold. For two local fluences, 650 and 900 J/m^2, the locations of the melting front and the void-free layers are marked without showing the corresponding snapshots. The velocities of the top void-free layers at 150 ps are provided in the figure

ulation performed below the spallation threshold, at 650 J/m^2 (Fig. 2a), the black bar shows the thickness of the void-free layer at 150 ps.

The representation of the simulation results in Fig. 16 clearly shows two distinct sections within the laser spot: (1) the central section of the spot, where the overheated top part of the surface region undergoes an explosive decomposition into vapor and liquid droplets, and (2) the periphery of the spot, where spallation of well-defined liquid layers connected to the bulk of the target by transient foamy structures of interconnected liquid regions is observed. While flat liquid layers are spalled from the target in individual simulations, the integral picture of ablation by the Gaussian laser beam is likely to involve a peel off of a continuous liquid layer with thickness increasing with increasing distance from the center of the laser spot, as shown schematically in Fig. 16 by the two gray stripes. The occurrence of both spallation and phase explosion processes within the same laser spot can be related to the results of pump-probe experiments [47,94,95], where the observation of optical interference patterns (Newton rings) can be explained by the spallation of a thin liquid layer from the irradiated target [21,28,29,93,123] and the disappearance of the interference fringes in the central part of the laser spot [47,94,95] can be attributed to the transition to the phase explosion regime.

Another effect related to the onset of the phase explosion in the central part of the laser spot is the sharp increase in the density of vapor emitted from the opening in the spalled layer, Fig. 16. The sharp, threshold-like increase in the fraction of the vapor-phase atoms in the ablation plume upon the transition from spallation to phase explosion has been observed in earlier simulations performed for Ni [21] and Cr [23] targets. This increase can be related to the results of plume imaging experiments [105], where the maximum

ejection of nanoparticles in laser ablation of Ni targets is observed at low fluences, whereas the degree of the plume atomization increases at higher fluences.

The melting depth shown by the red line connecting the red dots in Fig. 16 exceeds 200 nm near the center of the laser spot and decreases with increasing distance from the center. The pressure exerted by the expanding ablation plume on the underlying melted part of the target can cause a redistribution of the melt and formation of a rim of resolidified material along the edges of the laser spot [124–126], as well as an expulsion of the melt [111,125–127]. The melt expulsion may be responsible for the ejection of liquid droplets [128] that could significantly contribute to the total ablation yield at laser fluences exceeding the threshold for the phase explosion. Although the absence of the pressure gradients in the lateral directions prevents the direct observation of the effect of the melt expulsion in MD simulations, the variation of the characteristics of the ablation process within the laser spot, illustrated in Fig. 16, strongly suggests [21] the relevance of this mode of material ejection (melt expulsion or splashing by the recoil pressure exerted by ablation plume in the phase explosion regime) to femtosecond and picosecond laser ablation of metals.

7 Summary

The results of large-scale massively parallel atomistic simulations of femtosecond laser interactions with Al target provide a comprehensive picture of the microscopic mechanisms responsible for the material ejection in the spallation and phase explosion regimes. The relatively large lateral size of the computational systems used in the simulations ensures a realistic representation of the evolution of multiple voids generated in a sub-surface region of the irradiated target in the spallation regime and enables a detailed characterization of the ablation plume generated in the phase explosion regime.

The simulations performed in the spallation regime, when the material ejection and/or target modification are largely defined by the relaxation of laser-induced stresses, reveal the dependence of the void evolution and the parameters of the spalled layers on laser fluence. In a narrow range of fluences just below the spallation threshold, simulations predict a transient appearance of voids in the melted surface region of the target, followed by the void collapse or capture by resolidification process. Above the spallation threshold, the growth, coalescence and eventual percolation of multiple voids result in the separation (or spallation) of a thin liquid layer from the bulk of the target. The generation of voids is not localized within a well-defined "spall plane" but is taking place within a broad region that experiences growth of the magnitude of the tensile stresses and extends down to about 100 nm below the surface. Upon the expansion, this region transforms into a transient foamy liquid structure that extends between the spalled layer and the bulk of the target and eventually breaks and releases the spalled layer into free flight. The ejection velocity of the spalled layers ranges from ~300 m/s close to the spallation threshold to ~1,000 m/s at a laser fluence about 60 % above the spallation thresholds, whereas the thickness of the spalled layer decreases from 50 to 24 nm within the same range of fluences. An application of the thin film stability analysis to the spalled layers suggests that the layers are likely to decompose into liquid droplets with size on the order of hundreds of nanometers.

An increase of laser fluence up to more than 2.5 times the spallation threshold is found to result in the transition to the phase explosion regime, where the top part of the target undergoes an explosive decomposition into vapor and small clusters/droplets. The transition to the phase explosion regime is signified by a change in the composition of the ejected ablation plume from large liquid droplets to a mixture of vapor-phase atoms and clusters of different sizes. The ablation plume ejected in the phase explosion regime is characterized by spatial segregation of clusters of different sizes, with only small atomic clusters present in the front part of the plume that expands with velocity of up to 8–10 km/s, followed by slower medium-size clusters (101 to 10,000 atoms) that have ejection velocities of less than 4 km/s and droplets consisting of more than 10,000 atoms (diameters larger than 7 nm) that move with velocities of less than 3 km/s.

Despite being ejected from deeper regions under the surface, where the energy density is lower, the larger clusters/droplets have higher internal temperatures than the small clusters, e.g., the average internal temperature is more than 4,000 K for droplets consisting of more than 10,000 atoms and less than 3,000 K for clusters consisting of less than 50 atoms. The strong correlation of the internal temperature with the size (and the depth of origin) of a cluster can be attributed to a more efficient cooling of the top part of the plume due to the explosive decomposition and fast expansion of the mixture of vapor and small clusters as compared to a slower evaporative cooling of the large clusters/droplets in the tail of the ablation plume.

The overall cluster composition of the ablation plume is characterized by cluster size distributions which exhibit power law dependences of the probability to find a cluster of a given mass with power law exponents different for small (less than 20 atoms) and larger clusters. The decay of the probability with mass is slower for the larger clusters, i.e., the absolute value of the power law exponent is smaller. Despite the small number of large clusters/droplets, they constitute a major fraction of the total mass of ejected material. In the simulation performed close to the threshold for the phase explosion, the liquid particles with diameters larger than 7 nm

account for 93.9 % of the total mass of the ejected plume, whereas the contribution of the vapor-phase atoms is only 2.3 %.

Although a direct simulation of processes occurring on the scale of the whole laser spot is not possible with MD technique, a "mosaic approach" combining the results of a series of TTM-MD simulations performed for different laser fluences is used to discuss the possible collective effects occurring at the scale of the laser spot. In particular, the simultaneous occurrence of spallation and phase explosion in different parts of a spot irradiated by a Gaussian laser beam, as well as the effect of the melt expulsion due to the recoil pressure exerted by ablation plume, is discussed based on the simulation results.

Many of the results of the TTM-MD simulations of laser interactions with Al targets have striking similarity to the results reported earlier for different target materials, from molecular systems to metals and semiconductors. In particular, the physical conditions defining the onset of photomechanical spallation and the transition from the spallation to the phase explosion regime are found to be similar for a broad class of target materials. Moreover, some of the quantitative characteristics of laser-induced processes, such as the evolution of the void size distributions in spallation, the parameters of cluster size distributions and the degree of segregation of clusters and liquid droplets of different sizes in ablation plumes generated in the phase explosion regime are also surprisingly similar for different materials, reflecting the common mechanical and thermodynamic origins of the underlying processes.

Acknowledgments Financial support for this work was provided by the National Science Foundation (NSF) through Grants DMR-0907247 and CMMI-1301298, Electro Scientific Industries, Inc., and the Air Force Office of Scientific Research through Grant FA9550-10-1-0541. Computational support was provided by the Oak Ridge Leadership Computing Facility (projects MAT048) and NSF through the Extreme Science and Engineering Discovery Environment (project TG-DMR110090).

References

1. B.N. Chichkov, C. Momma, S. Nolte, F. von Alvensleben, A. Tünnermann, Appl. Phys. A **63**, 109 (1996)
2. S.-S. Wellershoff, J. Hohlfeld, J. Güdde, E. Matthias, Appl. Phys. A **69**, S99 (1999)
3. R.L. Harzic, N. Huot, E. Audouard, C. Jonin, P. Laporte, Appl. Phys. Lett. **80**, 3886 (2002)
4. A.Y. Vorobyev, C. Guo, Appl. Phys. A **86**, 321 (2007)
5. Q.-Z. Zhao, S. Malzer, L.-J. Wang, Opt. Express **15**, 15741 (2007)
6. Y. Dai, M. He, H. Bian, B. Lu, X. Yan, G. Ma, Appl. Phys. A **106**, 567 (2012)
7. S. Barcikowski, A. Hahn, A.V. Kabashin, B.N. Chichkov, Appl. Phys. A **87**, 47 (2007)
8. J. Perriere, C. Boulmer-Leborgne, R. Benzerga, S. Tricot, J. Phys. D: Appl. Phys. **40**, 7069 (2007)
9. N. Haustrup, G.M. O'Connor, Appl. Phys. Lett. **101**, 263107 (2012)
10. A. Miotello, N. Patel, Appl. Surf. Sci. **278**, 19 (2013)
11. P.L. Silvestrelli, A. Alavi, M. Parrinello, D. Frenkel, Phys. Rev. Lett. **77**, 3149 (1996)
12. V. Recoules, J. Clérouin, G. Zérah, P.M. Anglade, S. Mazevet, Phys. Rev. Lett. **96**, 055503 (2006)
13. Z. Lin, L.V. Zhigilei, V. Celli, Phys. Rev. B **77**, 075133 (2008)
14. H.O. Jeschke, M.S. Diakhate, M.E. Garcia, Appl. Phys. A **96**, 33 (2009)
15. Z. Lin, R.E. Allen, J. Phys.: Condens. Matter **21**, 485503 (2009)
16. C.F. Richardson, P. Clancy, Mol. Sim. **7**, 335 (1991)
17. X. Wang, X. Xu, J. Heat Transfer **124**, 265 (2002)
18. D.S. Ivanov, L.V. Zhigilei, Phys. Rev. B **68**, 064114 (2003)
19. D.S. Ivanov, L.V. Zhigilei, Phys. Rev. Lett. **91**, 105701 (2003)
20. Z. Lin, L.V. Zhigilei, Phys. Rev. B **73**, 184113 (2006)
21. L.V. Zhigilei, Z. Lin, D.S. Ivanov, J. Phys. Chem. C **113**, 11892 (2009)
22. Z. Lin, E.M. Bringa, E. Leveugle, L.V. Zhigilei, J. Phys. Chem. C **114**, 5686 (2010)
23. E.T. Karim, Z. Lin, L.V. Zhigilei, AIP Conf. Proc. **1464**, 280 (2012)
24. Z. Lin, R.A. Johnson, L.V. Zhigilei, Phys. Rev. B **77**, 214108 (2008)
25. D.S. Ivanov, Z. Lin, B. Rethfeld, G.M. O'Connor, Th.J. Glynn, L.V. Zhigilei, J. Appl. Phys. **107**, 013519 (2010)
26. C. Wu, D.A. Thomas, Z. Lin, L.V. Zhigilei, Appl. Phys. A **104**, 781 (2011)
27. L.V. Zhigilei, B.J. Garrison, J. Appl. Phys. **88**, 1281 (2000)
28. S.I. Anisimov, V.V. Zhakhovskii, N.A. Inogamov, K. Nishihara, A.M. Oparin, Yu.V. Petrov, JETP Lett. **77**, 606 (2003)
29. E. Leveugle, D.S. Ivanov, L.V. Zhigilei, Appl. Phys. A **79**, 1643 (2004)
30. L.V. Zhigilei, D.S. Ivanov, E. Leveugle, B. Sadigh, E.M. Bringa, Proc. SPIE **5448**, 505 (2004)
31. A.K. Upadhyay, H.M. Urbassek, J. Phys. D: Appl. Phys. **38**, 2933 (2005)
32. A.K. Upadhyay, N.A. Inogamov, B. Rethfeld, H.M. Urbassek, Phys. Rev. B **78**, 045437 (2008)
33. B.J. Demaske, V.V. Zhakhovsky, N.A. Inogamov, I.I. Oleynik, Phys. Rev. B **82**, 064113 (2010)
34. S.I. Ashitkov, N.A. Inogamov, V.V. Zhakhovskii, Yu.N. Emirov, M.B. Agranat, I.I. Oleinik, S.I. Anisimov, V.E. Fortov, JETP Lett. **95**, 176 (2012)
35. E. Ohmura, I. Fukumoto, Int. J. Japan Soc. Prec. Eng. **30**, 128 (1996)
36. L.V. Zhigilei, P.B.S. Kodali, B.J. Garrison, J. Phys. Chem. B **101**, 2028 (1997)
37. R.F.W. Herrmann, J. Gerlach, E.E.B. Campbell, Appl. Phys. A **66**, 35 (1998)
38. X. Wu, M. Sadeghi, A. Vertes, J. Phys. Chem. B **102**, 4770 (1998)
39. C. Schäfer, H.M. Urbassek, L.V. Zhigilei, Phys. Rev. B **66**, 115404 (2002)
40. L.V. Zhigilei, Appl. Phys. A **76**, 339 (2003)
41. L.V. Zhigilei, E. Leveugle, B.J. Garrison, Y.G. Yingling, M.I. Zeifman, Chem. Rev. **103**, 321 (2003)
42. P. Lorazo, L.J. Lewis, M. Meunier, Phys. Rev. Lett. **91**, 225502 (2003)
43. N.N. Nedialkov, P.A. Atanasov, S.E. Imamova, A. Ruf, P. Berger, F. Dausinger, Appl. Phys. A **79**, 1121 (2004)
44. C. Cheng, X. Xu, Phys. Rev. B **72**, 165415 (2005)
45. P. Lorazo, L.J. Lewis, M. Meunier, Phys. Rev. B **73**, 134108 (2006)
46. S. Amoruso, R. Bruzzese, X. Wang, N.N. Nedialkov, P.A. Atanasov, J. Phys. D: Appl. Phys. **40**, 331 (2007)

47. M.B. Agranat, S.I. Anisimov, S.I. Ashitkov, V.V. Zhakhovskii, N.A. Inogamov, K. Nishihara, Yu.V. Petrov, V.E. Fortov, V.A. Khokhlov, Appl. Surf. Sci. **253**, 6276 (2007)
48. E. Leveugle, L.V. Zhigilei, J. Appl. Phys. **102**, 074914 (2007)
49. M. Prasad, P. Conforti, B.J. Garrison, J. Appl. Phys. **101**, 103113 (2007)
50. L. Zhang, X. Wang, Appl. Surf. Sci. **255**, 3097 (2008)
51. M. Gill-Comeau, L.J. Lewis, Phys. Rev. B **84**, 224110 (2011)
52. L.V. Zhigilei, A.N. Volkov, E. Leveugle, M. Tabetah, Appl. Phys. A **105**, 529 (2011)
53. S. Sonntag, C. Trichet Paredes, J. Roth, H.-R. Trebin, Appl. Phys. A **104**, 559 (2011)
54. G. Norman, S. Starikov, V. Stegailov, V. Fortov, I. Skobelev, T. Pikuz, A. Faenov, S. Tamotsu, Y. Kato, M. Ishino, M. Tanaka, N. Hasegawa, M. Nishikino, T. Ohba, T. Kaihori, Y. Ochi, T. Imazono, Y. Fukuda, M. Kando, T. Kawachi, J. Appl. Phys. **112**, 013104 (2012)
55. X. Li, L. Jiang, Appl. Phys. A **109**, 367 (2012)
56. R.K. Singh, J. Narayan, Phys. Rev. B **41**, 8843 (1990)
57. A. Peterlongo, A. Miotello, R. Kelly, Phys. Rev. E **50**, 4716 (1994)
58. J.R. Ho, C.P. Grigoropoulos, J.A.C. Humphrey, J. Appl. Phys. **78**, 4696 (1995)
59. X. Xu, G. Chen, K.H. Song, Int. J. Heat Mass Transfer **42**, 1371 (1999)
60. O.A. Bulgakova, N.M. Bulgakova, V.P. Zhukov, Appl. Phys. A **101**, 53 (2010)
61. K. Eidmann, J. Meyer-ter-Vehn, T. Schlegel, S. Huller, Phys. Rev. E **62**, 1202 (2000)
62. J.P. Colombier, P. Combis, F. Bonneau, R. Le Harzic, E. Audouard, Phys. Rev. B **71**, 165406 (2005)
63. A.N. Volkov, L.V. Zhigilei, J. Phys.: Conf. Ser. **59**, 640 (2007)
64. M.E. Povarnitsyn, T.E. Itina, K.V. Khishchenko, P.R. Levashov, Phys. Rev. Lett. **103**, 195002 (2009)
65. M.E. Povarnitsyn, T.E. Itina, P.R. Levashov, K.V. Khishchenko, Phys. Chem. Chem. Phys. **15**, 3108 (2013)
66. L.V. Zhigilei, Z. Lin, D.S. Ivanov, E. Leveugle, W.H. Duff, D. Thomas, C. Sevilla, S.J. Guy, in *Laser-Surface Interactions for New Materials Production: Tailoring Structure and Properties*, ed. by A. Miotello and P. M. Ossi. Springer Series in Materials Science, vol. 130 (Springer, New York, 2010), pp. 43–79
67. L.V. Zhigilei, E. Leveugle, D.S. Ivanov, Z. Lin, A.N. Volkov, in *Nanosized Material Synthesis by Action of High-Power Energy Fluxes on Matter* (Siberian Branch of the Russian Academy of Sciences, Novosibirsk, 2010), pp. 147–220 (in Russian)
68. C. Wu, E.T. Karim, A.N. Volkov, L.V. Zhigilei, in *Lasers in Materials Science*, ed. by P. M. Ossi, M. Castillejo, L. V. Zhigilei. Springer Series in Materials Science, vol. 191 (Springer, New York, 2014)
69. A. Miotello, R. Kelly, Appl. Phys. A **69**, S67 (1999)
70. N.M. Bulgakova, A.V. Bulgakov, Appl. Phys. A **73**, 199 (2001)
71. B.J. Garrison, T.E. Itina, L.V. Zhigilei, Phys. Rev. E **68**, 041501 (2003)
72. S.I. Anisimov, B.L. Kapeliovich, T.L. Perel'man, Sov. Phys. JETP **39**, 375 (1974)
73. L.V. Zhigilei, B.J. Garrison, Mat. Res. Soc. Symp. Proc. **538**, 491 (1999)
74. C. Schafer, H.M. Urbassek, L.V. Zhigilei, B.J. Garrison, Comput. Mater. Sci. **24**, 421 (2002)
75. Y. Mishin, D. Farkas, M.J. Mehl, D.A. Papaconstantopoulos, Phys. Rev. B **59**, 3393 (1999)
76. G.P. Purja Pun, Y. Mishin, Phil. Mag. **89**, 3245 (2009)
77. R.W. Ohse, H. von Tippelskirch, High Temp. High Press. **9**, 367 (1977)
78. V. Morel, A. Bultel, B.G. Chéron, Int. J. Thermophys. **30**, 1853 (2009)
79. N. Tsakiris, L.J. Lewis, Eur. Phys. J. B **86**, 313 (2013)
80. http://www.faculty.virginia.edu/CompMat/electron-phonon-coupling/
81. R.H.M. Groeneveld, R. Sprik, A. Lagendijk, Phys. Rev. B **51**, 11433 (1995)
82. K.C. Mills, B.J. Monaghan, B.J. Keene, Int. Mater. Rev. **41**, 209 (1996)
83. G. Tas, H.J. Maris, Phys. Rev. B **49**, 15049 (1994)
84. J. Hohlfeld, S.-S. Wellershoff, J. Güdde, U. Conrad, V. Jähnke, E. Matthias, Chem. Phys. **251**, 237 (2000)
85. D. Bäuerle, *Laser Processing and Chemistry* (Springer, Berlin, 2000)
86. B.J. Siwick, J.R. Dwyer, R.E. Jordan, R.J.D. Miller, Chem. Phys. **299**, 285 (2004)
87. N.W. Ashcroft, N.D. Mermin, *Solid State Physics* (Holt, Rinehart and Winston, New York, 1976)
88. M.A. Bhatia, K.N. Solanki, A. Moitra, M.A. Tschopp, Metall. Mater. Trans. A **44**, 617 (2013)
89. J.-M. Savolainen, M.S. Christensen, P. Balling, Phys. Rev. B **84**, 193410 (2011)
90. A. Strachan, T. Çağın, W.A. Goddard III, Phys. Rev. B **63**, 060103 (2001)
91. G. Paltauf, P.E. Dyer, Chem. Rev. **103**, 487 (2003)
92. E. Leveugle, L.V. Zhigilei, Appl. Phys. A **79**, 753 (2004)
93. K. Sokolowski-Tinten, J. Bialkowski, A. Cavalleri, D. von der Linde, A. Oparin, J. Meyer-ter-Vehn, S.I. Anisimov, Phys. Rev. Lett. **81**, 224 (1998)
94. A.A. Ionin, S.I. Kudryashov, L.V. Seleznev, D.V. Sinitsyn, JETP Lett. **94**, 753 (2011)
95. A.A. Ionin, S.I. Kudryashov, L.V. Seleznev, D.V. Sinitsyn, A.F. Bunkin, V.N. Lednev, S.M. Pershin, JETP **116**, 347 (2013)
96. A. Vrij, Discuss. Faraday Soc. **42**, 23 (1966)
97. G.L. Klimchitskaya, U. Mohideen, V.M. Mostepanenko, Phys. Rev. A **61**, 062107 (2000)
98. J.M. Howe, *Interfaces in Materials: Atomic Structure, Thermodynamics and Kinetics of Solid–Vapor, Solid–Liquid and Solid–Solid Interfaces* (Wiley, New York, 1997)
99. L.V. Zhigilei, Mater. Res. Soc. Symp. Proc. **677**, AA2.1.1–AA2.1.11 (2001)
100. T.E. Itina, K. Gouriet, L.V. Zhigilei, S. Noël, J. Hermann, M. Sentis, Appl. Surf. Sci. **253**, 7656 (2007)
101. T.E. Itina, L.V. Zhigilei, J. Phys.: Conf. Ser. **59**, 44 (2007)
102. M.I. Zeifman, B.J. Garrison, L.V. Zhigilei, Appl. Surf. Sci. **197–198**, 27 (2002)
103. M.I. Zeifman, B.J. Garrison, L.V. Zhigilei, J. Appl. Phys. **92**, 2181 (2002)
104. S. Noël, J. Hermann, T. Itina, Appl. Surf. Sci. **253**, 6310 (2007)
105. S. Amoruso, R. Bruzzese, C. Pagano, X. Wang, Appl. Phys. A **89**, 1017 (2007)
106. S. Amoruso, R. Bruzzese, X. Wang, J. Xia, Appl. Phys. Lett. **92**, 041503 (2008)
107. O. Albert, S. Roger, Y. Glinec, J.C. Loulergue, J. Etchepare, C. Boulmer-Leborgne, J. Perriere, E. Millon, Appl. Phys. A **76**, 319 (2003)
108. N. Jegenyes, J. Etchepare, B. Reynier, D. Scuderi, A. Dos-Santos, Z. Tóth, Appl. Phys. A **91**, 385 (2008)
109. Y. Okano, K. Oguri, T. Nishikawa, H. Nakano, Appl. Phys. Lett. **89**, 221502 (2006)
110. H. Nakano, K. Oguri, Y. Okano, T. Nishikawa, Appl. Phys. A **101**, 523 (2010)
111. I. Apitz, A. Vogel, Appl. Phys. A **81**, 329 (2005)
112. T. Donnelly, J.G. Lunney, S. Amoruso, R. Bruzzese, X. Wang, X. Ni, J. Appl. Phys. **108**, 043309 (2010)
113. E. Leveugle, L.V. Zhigilei, A. Sellinger, J.M. Fitz-Gerald, Appl. Surf. Sci. **253**, 6456 (2007)
114. K.B. Shepard, C.B. Arnold, R.D. Priestley, Appl. Phys. Lett. **103**, 123105 (2013)

115. S.-H. Lai, K.-H. Chang, J.-L. Lin, C.-L. Wu, C.-H. Chen, Chem. Phys. Lett. **561–562**, 142 (2013)
116. H.M. Urbassek, Nucl. Instrum. Methods Phys. Res. B **31**, 541 (1988)
117. A. Bershadskii, Eur. Phys. J. B **14**, 323 (2000)
118. J.A. Aström, R.P. Linna, J. Timonen, P.F. Möller, L. Oddershede, Phys. Rev. E **70**, 026104 (2004)
119. G. Timár, J. Blömer, F. Kun, H.J. Herrmann, Phys. Rev. Lett. **104**, 095502 (2010)
120. I.S. Bitensky, E.S. Parilis, Nucl. Instrum. Methods Phys. Res. B **21**, 26 (1987)
121. L.E. Rehn, R.C. Birtcher, P.M. Baldo, A.W. McCormick, L. Funk, Nucl. Instrum. Methods Phys. Res. B **212**, 326 (2003)
122. O. Durand, L. Soulard, J. Appl. Phys. **111**, 044901 (2012)
123. N.A. Inogamov, Y.V. Petrov, S.I. Anisimov, A.M. Oparin, N.V. Shaposhnikov, D. von der Linde, J. Meyer-ter-Vehn, JETP Lett. **69**, 310 (1999)
124. J. Yang, Y. Zhao, N. Zhang, Y. Liang, M. Wang, Phys. Rev. B **76**, 165430 (2007)
125. V.V. Semak, J.G. Thomas, B.R. Campbell, J. Phys. D: Appl. Phys. **37**, 2925 (2004)
126. A. Ben-Yakar, A. Harkin, J. Ashmore, R.L. Byer, H.A. Stone, J. Phys. D: Appl. Phys. **40**, 1447 (2007)
127. M. von Allmen, J. Appl. Phys. **47**, 5460 (1976)
128. B. Liu, Z. Hu, Y. Che, Y. Chen, X. Pan, Appl. Phys. Lett. **90**, 044103 (2007)